Systematics of electronic and magnetic properties in the transition metal doped Sb_2Te_3 quantum anomalous Hall platform

M. F. Islam and C. M. Canali*
Department of Physics and Electrical Engineering, Linnaeus University, 391 82 Kalmar, Sweden

A. Pertsova and A. Balatsky
Nordita, Roslagstullsbacken 23, SE-106 91 Stockholm, Sweden

S. K. Mahatha, C. Carbone, and A. Barla
Istituto di Struttura della Materia (ISM), Consiglio Nazionale delle Ricerche (CNR), I-34149 Trieste, Italy

K. A. Kokh and O. E. Tereshchenko
Novosibirsk State University, 630090 Novosibirsk, Russia

E. Jiménez and N. B. Brookes
European Synchrotron Radiation Facility, 71 Avenue des Martyrs, Grenoble, France

P. Gargiani and M. Valvidares
ALBA Synchrotron Light Source, E-08290 Cerdanyola del Vallès, Spain

S. Schatz, T. R. F. Peixoto,† H. Bentmann,‡ and F. Reinert
Physikalisches Institut, Experimentelle Physik VII, Universität Würzburg, Am Hubland, D-97074 Würzburg, Germany

J. Jung, T. Bathon, K. Fauth, M. Bode, and P. Sessi§
Physikalisches Institut, Experimentelle Physik II, Universität Würzburg, Am Hubland, D-97074 Würzburg, Germany

(Received 13 February 2018; published 23 April 2018)

The quantum anomalous Hall effect (QAHE) has recently been reported to emerge in magnetically doped topological insulators. Although its general phenomenology is well established, the microscopic origin is far from being properly understood and controlled. Here, we report on a detailed and systematic investigation of transition metal (TM) doped Sb_2Te_3. By combining density functional theory calculations with complementary experimental techniques, i.e., scanning tunneling microscopy, resonant photoemission, and x-ray magnetic circular dichroism, we provide a complete spectroscopic characterization of both electronic and magnetic properties. Our results reveal that the TM dopants not only affect the magnetic state of the host material, but also significantly alter the electronic structure by generating impurity-derived energy bands. Our findings demonstrate the existence of a delicate interplay between electronic and magnetic properties in TM doped topological insulators. In particular, we find that the fate of the topological surface states critically depends on the specific character of the TM impurity: while V- and Fe-doped Sb_2Te_3 display resonant impurity states in the vicinity of the Dirac point, Cr and Mn impurities leave the energy gap unaffected. The single-ion magnetic anisotropy energy and easy axis, which control the magnetic gap opening and its stability, are also found to be strongly TM impurity dependent and can vary from in plane to out of plane depending on the impurity and its distance from the surface. Overall, our results provide general guidelines for the realization of a robust QAHE in TM doped Sb_2Te_3 in the ferromagnetic state.

DOI: 10.1103/PhysRevB.97.155429

I. INTRODUCTION

Topological insulators (TIs) represent a new state of matter [1,2]. They behave like insulators in the bulk, but are characterized by a nontrivial symmetry inversion at the band gap due to strong spin-orbit coupling. This gives rise to gapless conducting spin-helical states on their boundaries (edges or surfaces), with linear (Dirac) energy-momentum dispersion inside the bulk band gap, crossing at the Dirac point. The level degeneracy at the Dirac point is topologically protected by time-reversal symmetry.

External perturbations that break this symmetry can open an energy gap at the Dirac point and modify the spin texture, resulting in several novel quantum phenomena, possibly relevant

*carlo.canali@lnu.se
†Thiago.Peixoto@physik.uni-wuerzburg.de
‡hendrik.bentmann@physik.uni-wuerzburg.de
§sessi@physik.uni-wuerzburg.de

for spintronic and magnetoelectronic applications. Among these, one of the most interesting phenomena is the quantum anomalous Hall effect (QAHE). The idea of a quantum version of the anomalous Hall effect, i.e., a quantum Hall effect in the absence of external magnetic field and Landau levels, had already been suggested by Haldane [3] in 1988 but never realized until recently.

Soon after the discovery of three-dimensional TIs, it was predicted theoretically that the QAHE should occur in thin films of magnetic TIs [4]. Key elements leading to the QAHE are the opening of a magnetic energy gap at the Dirac point of the topological surface state and the positioning of the Fermi level inside this gap. The currently most discussed approach for engineering a gap is magnetic doping: ferromagnetically ordered magnetic dopants produce a net magnetization which breaks time-reversal symmetry and, when directed orthogonal to the TI surface, opens a gap in the TI surface states [5,6]. The theoretical prediction of the QAHE was first verified experimentally [7] in 2013 and since then it has been confirmed by several other groups (for a recent review, see Ref. [8]).

However, several outstanding problems remain and make the QAHE one of the presently most investigated topics of TI research [9–12]. For example, the nature of magnetic order in these systems is not well understood. Furthermore, although a precise quantization of the Hall conductivity is achieved, a small but nonzero and unexplained dissipative longitudinal conductivity remains detectable [9,10,13–15]. Most importantly, the effect has so far been observed only at ultralow temperatures (typically <100 mK), i.e., well below the Curie temperature of the respective magnetic TI material. It is quite self-evident that all these issues are unavoidable side effects of the magnetic impurities, which are on one hand necessary to trigger magnetic order, but on the other hand also lead to unintended changes of the TI's electronic structure near the Dirac point [16].

Establishing ferromagnetic order in a TI with an out-of-plane easy axis is a challenging problem. Ideally, it is desirable to attain magnetic TIs with a high ferromagnetic transition temperature T_C, which can be controlled by the concentration of magnetic impurities. Since the discovery of TIs, considerable experimental effort has been dedicated to achieve long-range magnetic order in two prototypical TIs, Bi_2Se_3 and Bi_2Te_3, by doping with different TM atoms, such as Cr, Mn, or Fe, in both bulk and thin film geometries [17–27]. Significant theoretical work has also been undertaken to understand the mechanism of magnetism in transition metal (TM) doped TIs [28–43]. For some of the magnetic TIs where the QAHE has been observed, such as Cr-doped $(Bi,Sb)_2Te_3$, it has been proposed that the mechanism driving the ferromagnetic transition is based on the Van Vleck spin susceptibility [4]. For an alternative interpretation of the ordering mechanism in Cr-doped Sb_2Te_3, see a recent theoretical study published in Ref. [44]. However, theoretical [45] and experimental [11] work has shown that in V-doped $(Bi,Sb)_2Te_3$ (another magnetic TI where the QAHE has been observed) the exchange mechanism must be more complex than the Van Vleck picture considered so far, and competing coupling mechanisms involving superexchange mediated by p orbitals of the host atoms may be at play. For example, the presence of a high density of states near the Fermi level and the Dirac point, originating from the the $3d$ levels of the vanadium impurities, was recently demonstrated [11]. These observations are in agreement with the overwhelming majority of photoemission and scanning tunneling microscopy (STM) studies showing a gapless Dirac cone in magnetically doped TIs [16,22,31,46–52].

Yet, the presence of a finite density of states near the Dirac point in magnetic topological insulators exhibiting the QAHE seems to defy the established basic theoretical understanding of this effect. In an attempt to resolve this apparent contradiction, Sessi *et al.* [16], on the basis of STM data on V-doped Sb_2Te_3 and elaborating on previous theoretical work [53,54], proposed a scenario based on the dual nature of the magnetic TM dopants in a TI, which on one hand are expected to open a gap at the Dirac point but at the same time provide impurity states in the same energy region, such that eventually a gapless condition at the Dirac point is reestablished [16,55]. The observation of the QAHE is only made possible by the localized nature of the impurity states, which results in the emergence of a mobility gap in samples characterized by a gapless density of states [16].

Since the theory supporting this picture was based on a model Hamiltonian that does not distinguish among different TM impurities [16], it is important to carry out more detailed theoretical and experimental studies assessing the individual effect that specific TM elements have on the electronic and magnetic properties of the respective host TI. This is the scope of this paper. Specifically, we have carried out systematic first-principles studies of the electronic and magnetic properties of substitutional Cr, V, Fe, and Mn dopants in Sb_2Te_3 TI, both in bulk and on the surface. In particular, we have computed the magnetic anisotropy energy and the easy axis for these magnetic TIs. In consideration of the relevant role played by the p levels of the nearby host atoms in the exchange coupling, we have also evaluated the spin polarization of the Te and Sb atoms nearest to the TM impurity. Last but not least, we have focused on the fundamental issue of whether or not different TM dopants give rise to resonance impurity states in the gap close to the Dirac point.

These theoretical predictions will be compared with experimental findings obtained using complementary techniques. Scanning tunneling microscopy (STM) has been used to check the structural properties of the samples while scanning tunneling spectroscopy (STS) measurements allowed us to evidence the local perturbations induced by the dopants inside the bulk band gap. Resonant photoemission (resPES) has been used to map the chemical and orbital character of the bands. Finally, magnetic properties have been analyzed by x-ray magnetic circular dichroism (XMCD). This technique allowed us to investigate the emergence of long-range magnetic order and to identify the easy magnetization direction. Even more importantly, it granted direct access to the magnetic coupling between dopants and the elements of the host material, shedding light on the exchange mechanisms.

The paper is organized as follows. In Sec. II, we describe the results of our first-principles calculations of the electronic structure and magnetic properties of TM doped Sb_2Te_3, providing a theoretical framework to analyze and interpret the experimental studies. Crystal growth is described in Sec. III. Section IV presents the results of STM and STS measurements, focusing on the issue of the impurity resonances appearing in the bulk gap in the vicinity of the Dirac point. ResPES

measurements, providing direct experimental access to the 3*d* impurity states residing within the valence band, are discussed in Sec. V. Section VI deals with XMCD measurements, aimed at elucidating the microscopic magnetic characteristics of the TM dopants in the TI host, such as the magnetic moment, the anisotropy, and the induced spin polarization on host atoms by the magnetic dopants. Finally, in Sec. VII we summarize the main findings of our combined theoretical and experimental study, and discuss their implication for the realization of a robust QAHE regime in ferromagnetic Sb_2Te_3.

II. THEORETICAL STUDIES

A. Computational details

The density functional theory (DFT) calculations are performed using the full-potential all-electron linearized augmented plane-waves method as implemented in the state-of-the-art WIEN2K *ab initio* package [56]. The Perdew-Burke-Ernzerhof generalized gradient approximation (PBE-GGA) is used for the exchange correlation functional [57]. To investigate the trends of electronic properties of different TM impurities in Sb_2Te_3 we have constructed bulk and surface supercells (see Fig. 1) using experimental lattice parameters ($a = b = 4.264$ Å, $c = 30.457$ Å, $\gamma(\angle ab) = 120^\circ$) [58], with the c axis of the crystal (the z axis in our calculations) along the [001] direction. For bulk, we have constructed a $3 \times 3 \times 1$ supercell containing three quintuple layers (QLs) and a total of 135 atoms. For surface calculations we have considered a $3 \times 3 \times 2$ surface supercell, a slab of finite thickness consisting of six QLs grown along the [001] direction, which is perpendicular to the (111) surface of Sb_2Te_3. This supercell contains a total of 270 atoms. The slab's bottom and top (111) surfaces are terminated by Te layers. A vacuum of 15.87 Å is added along the surface direction to avoid supercell interaction.

Impurities are introduced by substituting one Sb atom per supercell with V, Cr, Mn, or Fe, respectively. As shown in the left panel of Fig. 1, bulk substitution is modeled by replacing an Sb atom in the middle of the supercell, corresponding to an impurity concentration of about 11% for the respective Sb layer and 1.8% for the entire supercell. For surface calculations, an impurity is added by substituting a Sb atom by a TM atom in the topmost Sb layer, which is the first layer under the very top surface Te layer. This doping also corresponds to an impurity concentration in the Sb layers of about 11% and 0.9% for the entire supercell. It should be noted that in this work we have not calculated averages over different chemical disorder realizations, which may be important for more accurate description of the system. However, since in this work, we are mainly interested in calculating the single-ion anisotropy, which primarily depends on the local environment of the impurity, the chemical disorder is not expected to play any significant role.

All calculations are performed after fully relaxing the atomic positions in all structures. The effect of relaxation is not very strong in Sb_2Te_3, both for bulk and surface. However, the nearest-neighbor Te atoms are observed to move slightly towards the TM impurity atom. The local symmetry of the impurity atom is approximately C_{3v} for both bulk and surface except that the distances between impurity and nearest-neighbor Te atoms are slightly different in bulk and surface. All the bulk calculations are performed using a $3 \times 3 \times 1$ k mesh, whereas for surface calculations we used $2 \times 2 \times 1$ k mesh in the Brillouin zone.

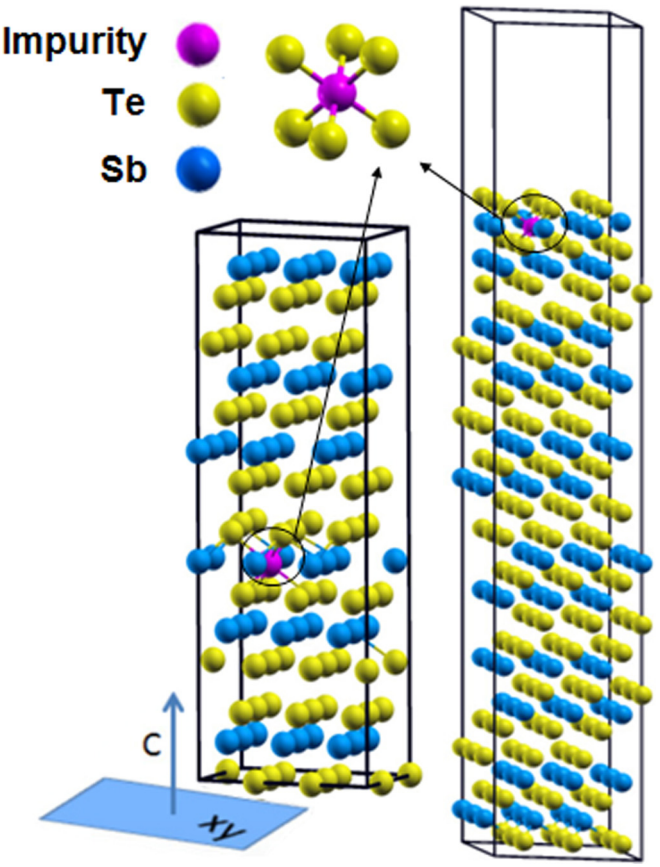

FIG. 1. Bulk (left panel) and surface (right panel) supercell of Sb_2Te_3 doped with a TM magnetic impurity substituting a Sb atom of the host material. The local symmetry of the impurity atom is C_{3v} for both bulk and surface case. For the surface supercell, the TM impurity is located on the first Sb monolayer under the top surface consisting of a Te monolayer. In the surface calculations, the slab thickness consists of six quintuple layers, grown along the C direction. The exposed top and bottom surfaces of the slab are (111) type.

The single-ion magnetic anisotropy energy (MAE) is calculated by using the force theorem in the presence of spin-orbit interaction, according to which the anisotropy energy for two magnetization directions of the TM impurity is the difference between the sum of all single-particle Kohn-Sham eigenvalues for the two directions [59]. In this work, we have calculated the energies for two magnetization directions, namely, the out-of-plane [001] direction (corresponding to the c axis in bulk) and the in-plane [110] direction (in the xy plane):

$$\mathrm{MAE} = \sum_{i,[001]}^{E_f} (\epsilon_{i\uparrow} + \epsilon_{i\downarrow}) - \sum_{i,[110]}^{E_f} (\epsilon_{i\uparrow} + \epsilon_{i\downarrow}). \qquad (1)$$

The magnetic anisotropy energy calculated in Eq. (1) is the magnetocrystalline anisotropy induced by the atomic spin-orbit coupling. It is important to emphasize that our first-principles DFT calculations of this quantity, carried out for

a slab of finite thickness, include automatically the effects of the symmetry breaking and atom relaxation occurring at the surface, which are responsible for the contribution to the magnetic anisotropy known as surface anisotropy. Therefore, although in our DFT calculations for a slab geometry we cannot disentangle bulk and surface anisotropy, the contribution coming from the latter is accounted for. The long-range dipole-dipole interaction, which is responsible for the shape anisotropy in thin films, is not explicitly included in the PBE exchange-correlation functional used in this work. However, this effect is expected to be rather small in the dilute magnetic system that we are considering.

Since WIEN2K is an all-electron code with plane-wave basis, the electronic and magnetic properties of a system can be calculated very accurately. The tradeoff is that the calculations carried out with this code is computationally extremely demanding, particularly for the large supercells considered in this work, both in terms memory and calculation time. For example, a typical surface calculation requires a total of about six weeks to attain a fully relaxed crystal structure in the presence of the TM impurity and to perform anisotropy calculations in a 20 core node with 64 GB memory (which is the maximum memory/node available in our supercomputer cluster at Lunarc).

Because of these computational constraints, most of the calculations in this work were carried out using GGA. For the case of V-doped Sb_2Te_3, we have also performed GGA + U calculations in order to study the effect of electronic correlation effects which may play a significant role, as indicated by the theoretical and experimental data presented below. DFT in the GGA + U implementation is a suitable approach to address this case. For these calculations, we have used $U = 4$ eV, which is the typical value for TM atoms [60].

B. Results

1. TM impurity magnetic moment and induced spin polarization of the host atoms

In pristine Sb_2Te_3, a semiconductor with bulk gap of $\approx$0.21 eV, the Sb cations are in the +3 oxidation state. The 3d TM impurities have an electronic configuration [Ar]3d^n4s^2, with $n = 3$ for V, $n = 4$ for Cr, $n = 5$ for Mn, and $n = 6$ for Fe. When a TM atom replaces an Sb atom in Sb_2Te_3, its possible oxidation states are either +3 or +2. In the first case, the TM atom donates the same number of electrons as the original Sb. For this oxidation state, which leads to the electronic configuration of [Ar]3d^{n-1}, the expected magnetic moment of the impurity would naively be $(n-1)\mu_B$. For the oxidation state +2, the electronic configuration of the impurity is [Ar]3d^n, resulting in a magnetic moment that should be close to the atomic value $n\mu_B$ for V, Cr, and Mn, and $(n-2)\mu_B$ for Fe, where the minority-spin levels start to be filled. Since in this case only two electrons of the TM impurity (the two 4s electrons) contribute to binding, a hole state is created in the host crystal, formed predominantly by the p states of the Te atoms nearest to the TM impurity atom with a small admixture of the impurity d states. The appearance of hole states localized on the NN anions and in part on the TM impurity is precisely what happens in the familiar case of Mn-doped GaAs, where Mn impurities substitute Ga atoms [61]. This p-d hybridization results in a partial spin polarization of the host p states, which can play an important role in determining the magnetic properties and the mechanism responsible for ferromagnetism of doped topological insulators.

TABLE I. Magnetic moments (in units of μ_B) for bulk and surface-doped Sb_2Te_3 for four different TM impurities. (The values for the case of surface impurities are in parentheses.) The first column displays the magnetic moment of the TM impurity. The second column is the value of the total magnetic moment induced by the TM impurity on its nearest-neighbor (NN) Te atoms. The +/− sign means that the direction of the induced moment is parallel/antiparallel to the impurity d moment, implying a ferromagnetic (FM)/antiferromagnetic (AFM) exchange coupling (see third column). The fourth column displays the exchange coupling (FM or AFM) between the TM impurity and its NN Sb atoms. Note that the sign of the exchange coupling is the same for bulk and surface doping.

	Magnetic moment (μ_B)			
Impurity type	Impurity	Induced moment on NN Te	Int. with NN Te	Int. with NN Sb
V	1.98 (2.00)	−0.27 (−0.20)	AFM	FM
Cr	3.02 (2.90)	−0.33 (−0.24)	AFM	FM
Mn	3.97 (4.12)	−0.17 (−0.03)	AFM	FM
Fe	3.20 (3.34)	+0.33 (0.24)	FM	FM

Table I shows calculated magnetic moments of impurity atoms (results for both bulk and surface impurities are displayed) together with the induced moment of the host atoms, along with the character of the magnetic coupling between the impurity, the nearest-neighbor (NN) Te atoms, and NN Sb atoms (which are the next-nearest-neighbor atoms to the TM impurity). The impurity magnetic moment for V is close to $2\,\mu_B$ for both bulk and surface doping, suggesting that substitutional V should be in the oxidation state +3. The same oxidation state +3 characterizes Cr impurities, for which the magnetic moment is found to be close to $3\,\mu_B$. In fact, a close inspection of the orbital occupancies for these impurities reveals that the electron occupation of the majority-spin 3d levels is close to 2.5 electrons for V and 3.4 electrons for Cr. At the same time, the minority-spin d levels, which are expected above the Fermi level, are occupied by approximately 0.5 electrons, as a result of their hybridization with the p levels of NN Te atoms. In both cases, the 4s levels have a very small electron occupation of $\leqslant$0.1.

Mn impurities are expected to be in the oxidation state +2, which is supported by the observation that the electron occupancy of the majority-spin 3d levels is 4.5. A net magnetic moment close to $4\,\mu_B$ shown in Table I is then the result of these majority electrons and the opposite contribution of $\approx$0.5 electrons occupying the minority-spin d orbitals due to the effect of p level hybridization. In contrast with the other impurities, Fe minority states start to be occupied even in the absence of hybridization with host atoms. Indeed, the analysis of the d level occupancy shows that Fe has 4.6 majority-spin electrons and 1.3 minority-spin electrons. This implies a total of six electrons occupying the d-level core, corresponding to an oxidation state of +2. The magnetic moment of Fe is therefore close to $3.3\,\mu_B$. These considerations on the oxidation state

of the TM impurities in Sb_2Te_3 are in good agreement with experimental results obtained for Bi_2Te_3 TI [62], which is isoelectronic to Sb_2Te_3.

The impurity magnetic moment induces a spin polarization on the nearby Te and Sb host atoms, the strength of which depends on the type of impurity involved. In bulk Sb_2Te_3, the induced moment at the NN Te sites is about $0.3\,\mu_B$ for V, Cr, and Fe, but less than $0.2\,\mu_B$ for Mn. On the surface, the impurity d states are more localized as compared to those in bulk because of the lower coordination. As a consequence, the p-d hybridization is smaller on the surface, resulting in smaller induced NN moments. Our calculations also show that the local moments of V, Cr, and Mn couple antiferromagnetically (AFM) with the induced moment at the NN Te sites, whereas Fe couples ferromagnetically (FM) with Te in both bulk and surface. However, the coupling between the impurity atom and the induced moment at the Sb sites is FM for all four impurities, consistent with experiment (see also discussion below) [16,27].

As mentioned above, and this will become more clear when we discuss the impurity-induced modification of local density of states (DOS), V-doped Sb_2Te_3 has a complex electronic structure with a substantial DOS at the Fermi level originating from the V d levels. It is therefore important to investigate how electronic correlations affect the electronic and magnetic properties of the system. For this purpose, we have investigated V dopants in bulk Sb_2Te_3 within the framework of GGA + U, with $U = 4.0$ eV. The effect of Hubbard U is to localize the d states of the V atom. Consequently, the local moment of V increases to $2.6\,\mu_B$. A closer inspection of the orbital occupancy shows that the enhanced magnetic moment is the result of an increase of the majority-spin occupancy from 2.5 to 2.8 and a simultaneous decrease of the minority-spin occupancy from 0.48 to 0.26. Since the hybridization of the d states of the V impurity with its neighboring atoms decreases with correlations, the induced moments at the NN Te sites decrease to $0.21\,\mu_B$. However, the magnetic coupling between V and its NN Te sites remains AFM as in the case of $U = 0$.

2. Magnetic anisotropy energy of TM impurities in Sb_2Te_3

According to a minimal two-dimensional continuum model, to open a gap at the DP in a magnetic TI, it is necessary that the magnetization is oriented along the normal of the TI surface [63–65]. The orientation of the magnetization is determined by the magnetic anisotropy energy (MAE) of the system. We have calculated both the bulk and surface MAE and the corresponding easy axes for all impurities studied in this work. The results are shown in Table II. The direction of easy axis depends on the type of impurity. For V, Cr, and Mn bulk impurities, the easy axis is out of plane, that is, along the the growth direction of the crystal cleavage plane, while for Fe it is within the surface plane. Our results show that the surface anisotropy may qualitatively differ from the corresponding bulk values. For example, V and Mn exhibit an easy axis within the surface plane, contrary to bulk, whereas the Cr easy axis is still out of plane, just like for bulk. These calculations suggest that only the ground state of Cr-doped Sb_2Te_3 can sustain a ferromagnetic order with out-of-plane magnetization, and therefore will open a magnetic gap at the DP.

TABLE II. Single-ion magnetic anisotropy energy (MAE) of different TM magnetic impurities in bulk and surface Sb_2Te_3 topological insulator. The out-of-plane easy axis in bulk is along the growth c direction of the crystal. For surface impurities, the out-of-plane easy axis is along the [001] direction, which is perpendicular to the exposed (111) surface, terminating the slab.

	Bulk		Surface	
Impurity type	MAE (meV)	Easy axis	MAE (meV)	Easy axis
V	0.07	c axis	0.45	In plane
Cr	0.43	c axis	0.41	Out of plane
Mn	0.58	c axis	0.65	In plane
Fe	0.20	xy plane	0.60	In plane

Whereas the calculated out-of-plane easy axis of Cr-doped Sb_2Te_3 agrees well with experiment [66], theoretical data for V-doped samples suggest an in-plane anisotropy for the surface layer which is not supported by the experiment (see also the discussion in Sec. VI) [9]. To understand this apparent discrepancy between the experimental measurement and the theoretical results, we would like to emphasize that in our DFT calculations the TM impurity has been added only to the topmost Sb layer (i.e., the first subsurface layer). Therefore, in our surface calculations we have not really considered any magnetic order originating from bulk doping. If bulk magnetic order is also achieved, it can act as an external magnetic field to the surface electrons and can significantly influence the anisotropic properties of the film. Thus, it might be possible that bulk magnetic order can change the orientation of magnetization produced by a single surface layer.

3. Resonances in bulk-doped Sb_2Te_3

As discussed in Sec. I, the presence of impurities can give rise to impurity resonances close to the DP, which can be detrimental on the observation of the QAHE. To investigate whether the TM impurities give rise to resonance states, we have first calculated the *bulk* density of states (DOS) for TM doped systems. In particular, we are interested in determining the position of the impurity states in the bulk gap relative to the Fermi level. The total density (top panel in each of the four subfigures) and the density of d states (bottom panel in each of the four subfigures) of various bulk dopants is plotted in Fig. 2. The most important feature shown in the figure is that for both V and Mn dopants there is a finite density of impurity states at the Fermi level in the form of a broad resonance state (the Fermi energy is the vertical dotted line in the figure). On the other hand, for Cr the Fermi level is just in the middle of the gap, which appears to remain free of resonance states. Impurity d-level states for Cr (see lower panel for the Cr case) all occur inside the bulk conduction band. Fe dopants are qualitatively similar to V, displaying a finite DOS at E_F originating from the minority-spin d levels. In contrast, Mn is qualitatively more similar to Cr, displaying only a small DOS at E_F, which however is located not in the middle of bulk gap as for Cr, but closer to the valence band edge.

Given the presence of impurity states in the gap for V dopants, it is important to assess the role played by electron

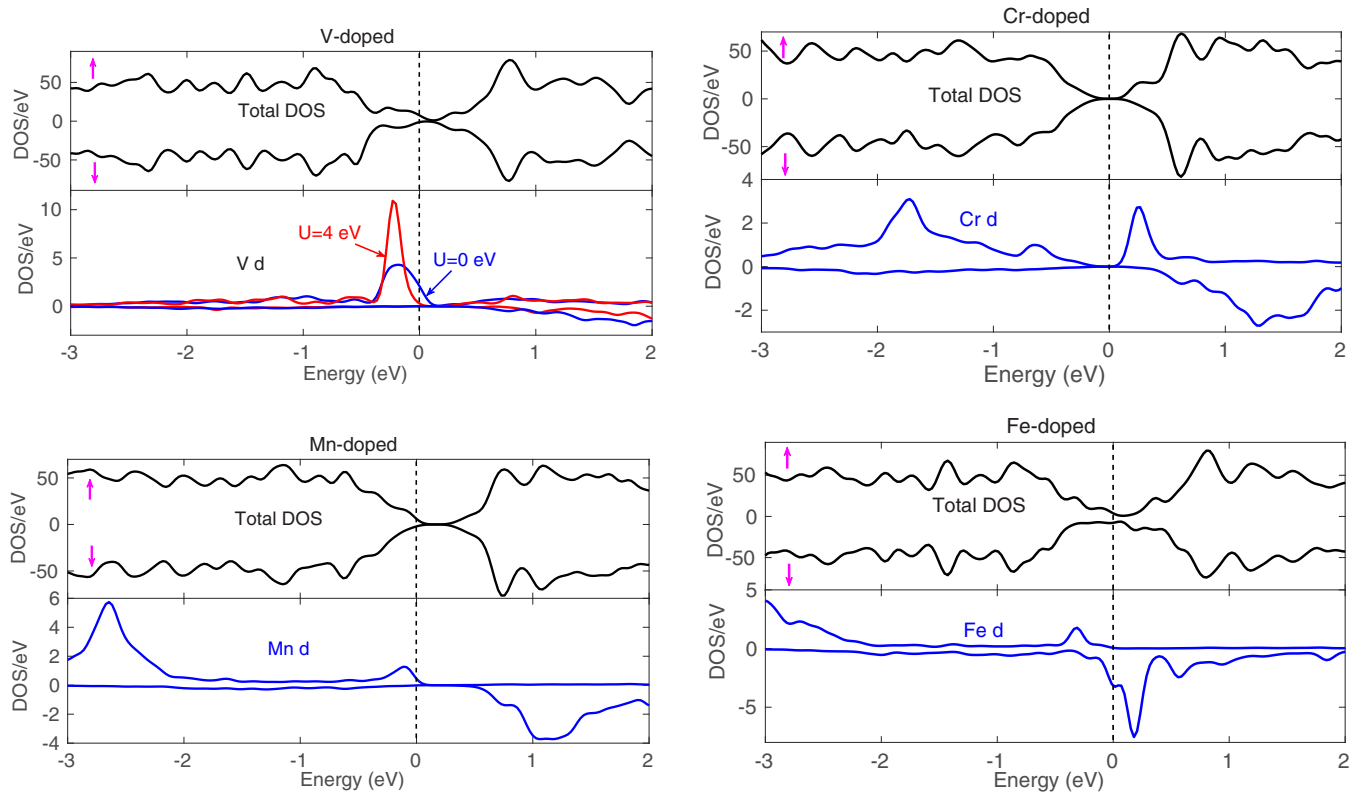

FIG. 2. Density of states of bulk TM doped Sb_2Te_3 for different bulk magnetic impurities. Top to bottom: V, Cr, Mn, Fe. For each impurity case, the black curve in the upper panel is the total DOS, while the blue curve in the lower panel represents the d-level DOS of the impurity. Positive and negative DOS values refer to majority- and minority-spin DOS, respectively. The vertical dotted line at zero energy marks the position of the Fermi level. The red curve for the V impurity is the d-level DOS obtained in a GGA + U calculations, with $U = 4$ eV. All other results are for $U = 0$.

correlations, which can modify the electronic structure of the impurity states. Therefore, we have carried out GGA + U calculations with $U = 4$ eV for V-doped Sb_2Te_3. The resulting V d-level DOS calculated is shown as a red line in Fig. 2 (top panel). As expected, the effect of the onsite Hubbard interaction U is to increase the localization of the d electrons around the impurity core. This is reflected in the d-level DOS of the majority spins, which are pushed further below the Fermi level, increasing their overall occupancy, as we have already seen above in the discussion of the magnetic moment. The resonant nature of these impurity states is enhanced by the correlations: the broad shoulder at the Fermi energy becomes a higher and narrower peak. However, it is important to note that, although correlations have the effect of reducing the d-level DOS at the Fermi energy, the DOS near E_F is still finite. Although not calculated explicitly here, previous calculations on TM doped Bi_2Se_3 show that the inclusion of Hubbard U has a very similar effect on the d-level DOS of other TM impurities [32]. In particular, we expect that correlations will produce minimal changes to the Cr d-level DOS, and by displacing the d levels in the way described above, will make the Mn DOS look even more similar to Cr. The case of Fe is a bit peculiar since the finite DOS in the absence of correlations is due to minority-spin d levels. However, it is likely that the effect of U, while pushing these levels further above E_F, will nevertheless maintain a finite, albeit small, DOS coming from these states. In conclusion, our calculations show that only for V and, to a lesser extent, Fe dopants resonant states are theoretically expected inside the bulk gap close to E_F. The DOS of these d levels remains finite even when electron correlations are included.

4. Resonances in surface-doped Sb_2Te_3

We now consider the case of TM magnetic impurities located on the (111) surface of Sb_2Te_3, focusing on their effect on the electronic DOS in the vicinity of the Dirac point. As explained in Sec. II A, the phrase *impurity located on the surface* is used to describe a TM atom that replaces an Sb atom in the topmost Sb layer, just underneath the Te layer terminating the supercell (see Fig. 1). This TM atom primarily hybridizes with the three NN Te atoms in the topmost layer and another three in the third layer. The penetration of the topological surface states inside the bulk material decays exponentially with the distance from the surface. More precisely, it is known that the decay length of the surface states is of the order of two to three quintuple layers (QLs) [67]. Therefore, we expect that the orbital levels of the TM impurity will overlap with and strongly affect the surface states of the top surface of the supercell. On the other hand, the TM impurity will have essentially no influence on the surface states of the bottom surface of the supercell, which is six QLs thick. The theoretical analysis of the TM impurities at the surface considered here is essential for the interpretation of the STM and XMCD experiments described below, which are mostly surface sensitive.

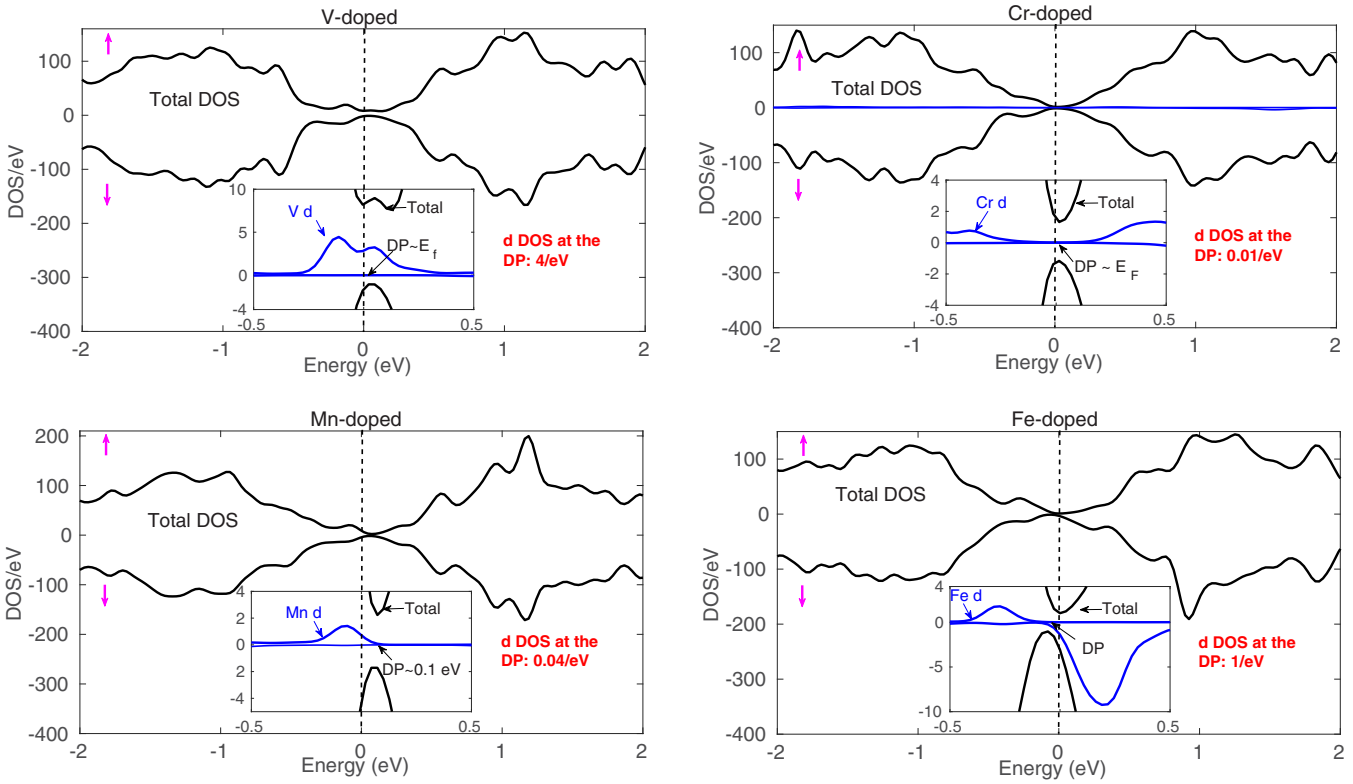

FIG. 3. Density of states of TM doped Sb_2Te_3 for different surface magnetic impurities. Top to bottom: V, Cr, Mn, and Fe. The vertical dotted line at zero energy marks the position of the Fermi level. The inset in each plot shows the DOS around the Dirac point (DP) of the top-surface states. The blue curve in this inset is the impurity d-level DOS. For all dopants the DP is very close to the Fermi level, with the exception of Mn, where the DP is ≈ 0.1 eV. The value of the impurity d-level DOS at the DP is indicated in red. For V there is a finite d-level DOS at the DP. On the other hand, for Cr the d-level DOS at the DP is essentially zero. Fe and Mn are somewhat in-between these two extremes, with Fe resembling V and Mn resembling Cr.

The DOS results of the surface impurity calculations are plotted in Fig. 3. Comparing with Fig. 2, it is evident that the impurity states for surface doping resemble in part the DOS for bulk doping. In order to identify the precise position of the DP relative to the Fermi level, the band structure is required. However, since we were unable to perform band-structure calculations for such a large supercell, due to the computational limitations explained in Sec. II A, the DP is estimated by assuming that the DOS is expected to be a minimum at the DP, as shown in Fig. 3. We would like to emphasize that the presence of a finite DOS around the DP of the top-surface states is due to the presence of the bottom-surface states at the same energies. Indeed, as shown in Ref. [32], when an impurity is positioned only on the top surface of a finite-thickness slab, inversion symmetry is broken, and the two Dirac cones of top and bottom surfaces are shifted with respect to each other. As a result, the energy region containing the DP of the top-surface states displays a finite DOS arising from the shifted surface states of the bottom surface.

For V-doped Sb_2Te_3, the impurity d states clearly lie not only inside the bulk gap, but also quite close to the DP of the surface states, in the energy region that should precisely correspond to a magnetic gap. This important theoretical result is consistent with experiment [16]. (Note that in our calculations the DP for V-doped Sb_2Te_3 essentially coincides with the Fermi level.) For Cr-doped Sb_2Te_3, the situation is quite different. As shown in the second panel of Fig. 3, in this case there are no impurity resonance states present within the bulk gap. The Fermi level lies just in the middle of this bulk gap, and it is very close to the DP. Thus, for this dopant, when the broken time-reversal symmetry of the magnetic state opens a magnetic gap at the DP, there will be no impurity states available to fill this gap. Most likely this is one of the main reasons why Cr-doped $(Bi,Sb)_2Te_3$, a TI with properties similar to Sb_2Te_3, remains one of the most suitable systems to realize the QAHE [7].

The case of Mn surface doping is displayed in the third panel of Fig. 3. Here, we can see that Mn impurities introduce a small albeit finite DOS at the Fermi level, which, as for the case of bulk impurities, is located close to the valence band edge. However, we find that the DP is located approximately at 0.1 eV above the Fermi level, where the contribution of Mn impurity states is essentially zero. Since the magnetic gap possibly opened by the time-reversal breaking perturbation is centered at the original DP of Sb_2Te_3, and is expected to be of the order of a couple of tens of meV at most, we conclude that in this case the Mn impurity states should not be able to fill this gap. Therefore, Mn-doped Sb_2Te_3 is in a way qualitatively similar to Cr-doped Sb_2Te_3, in that any magnetic gap opened by the impurity will not be affected by the presence of additional impurity resonances. Notice also that, on the basis of our analysis on the effect of correlations discussed in Fig. 2,

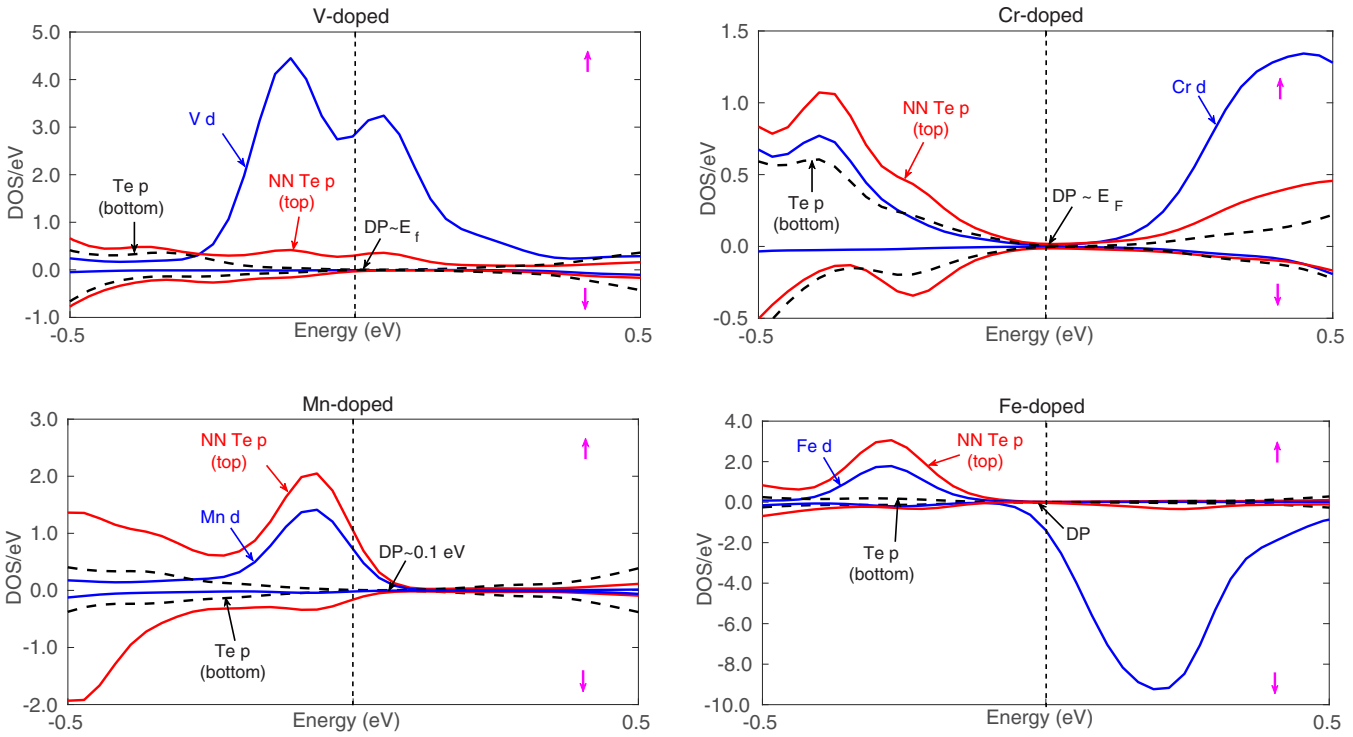

FIG. 4. Relative contribution of the impurity d-level DOS (blue curve) and the NN Te p-level DOS of the top surface (red curve) of Sb_2Te_3 for different surface magnetic doping. The Te p-level DOS of the top surface is strongly affected by the nearby impurity. In contrast, the Te p-level DOS of the bottom surface, also plotted as a comparison (black dashed line), is not influenced by the impurity.

we expect that the inclusion of onsite correlation effects via a Hubbard interaction U will further remove the small DOS from the gap region.

Finally, the case of Fe surface impurities is discussed in the bottom panel of Fig. 3. As for the case of bulk impurities, Fe is a bit different from the other three cases since the impurity-induced resonant levels inside the bulk gap now originate from minority-spin states. In this case, we find that the DP, which in our calculation occurs very close to the Fermi level, is located in a region where the d-level DOS is small but definitely finite, similarly to what happens with V. However, in contrast to the case of V, where the impurity states merge with the valence band edge, these states are now located in the middle of the bulk gap, and therefore resemble more properly an impurity band.

The different electronic behavior of the TM impurities inside the gap, already visible from the TM d-level impurity states, is also reflected in their coupling to the p levels of the NN Te atoms. In Fig. 4 we plot the DOS of the impurity d states together with the DOS of the p states of its NN Te atoms on the top surface. The position of the top-surface state's DP is indicated in the figure by a dashed vertical line. For comparison, we also plot the DOS of the p states of the Te atoms on the bottom surface, which are the NN of a Sb atom placed in the equivalent position of the one substituted with the impurity on the top surface. Since the impurity atoms are placed only in the topmost Sb layer (second layer from the top), only the top DP is influenced by the impurity, whereas the bottom DP remains unchanged. We note that while the contribution of p states of Te atoms at the bottom surface is very similar for all types of impurities, at the top surface the DOS of NN Te p states typically follows closely the impurity d states due to the p-d hybridization (with the exception of Fe), and therefore is quite different for different impurities. In particular, the striking difference between V and Cr, already observed in Fig. 3, is confirmed by these results. For V, there is a finite DOS of host p states around the Fermi level and the DP, which follows the same trend of the impurity d levels, and extends above the Fermi level. On the other hand, for Cr this p-level contribution from the NN Te atoms is totally absent at the DP. For Mn, the p-level DOS of the NN Te atoms follows closely the impurity d-level DOS. In particular, it is finite at the Fermi level, but negligible at the DP, which is about 0.1 eV above the Fermi level. Note that the behavior of the hybridized NN p levels, clearly giving rise to a hole state around the Fermi level, is similar to what happens for substitutional Mn impurities in GaAs [61].

Fe is again quite different from all other impurities, also concerning the p-d hybridization with the NN atoms. The bottom right panel of Fig. 4 shows that the finite DOS of minority-spin d-level impurity states in the vicinity of the DP does not result in any appreciable p-level contribution from the NN Te atoms. Substantial p-d hybridization takes place only with majority-spin states below the Fermi level, in an energy region far away from the DP. Therefore, for Fe, the impurity levels emerging in the crucial energy region around the DP, where a magnetic gap is likely to open, have mainly d character. These states tend to form an impurity band inside the bulk band gap, separated from the valence band top edge, and eventually merge with the conduction band bottom edge.

In summary, our calculations show that Mn- and Cr-doped Sb_2Te_3, in contrast with V-doped Sb_2Te_3, do not host any

resonance states in the energy region around the DP, where a magnetic gap in the surface states can be opened by the magnetic impurities. Our calculations also show a finite DOS of impurity levels at the DP for Fe-doped Sb_2Te_3; but, unlike V, these minority-spin states have essentially a *d* character, and do not hybridize with the *p* levels of the NN Te atoms of the host material.

Microscopically, any exchange interaction between topological surface and impurity states leading to a gap opening at the DP should require some kind of overlap and consequent hybridization between these two states. Indeed, in Ref. [32] a DFT band-structure calculation carried out Mn-doped Bi_2Se_3 showed that surface states are strongly hybridized with the impurity states, and this hybridization is crucial to open a gap at the Dirac point. Although not confirmed by similar band-structure calculations, the weak hybridization that we find for V would suggest that in this case, the size of the gap at the Dirac point should be rather small.

The theoretical considerations of QAHE discussed above are based on the existence of magnetic order only at the surface. Although it might be possible to observe QAHE with only bulk magnetic order with perpendicular anisotropy, the effect is likely to be smaller. A larger magnetic gap at the Dirac point (DP) is desirable for QAHE, which can be suitably achieved if surface is also magnetic with out-of-plane easy axis. In addition, some calculations show that the critical temperature T_C for bulk magnetic order is considerably smaller than that of the surface magnetic order [43]. Therefore, the T_c for the QAHE will also be lower when only bulk magnetization is present, without surface magnetic order.

We conclude this section with a few considerations on the possible nature of the exchange coupling and the ensuing mechanism of magnetic order in Sb_2Te_3 for different dopant species. The presence of a finite density of impurity *d* and host *p* states around the Fermi level for V and the absence of these states for Cr suggests that the mechanism of magnetism is likely to be quite different for V-doped and Cr-doped Sb_2Te_3. In the case of V, the impurity states tend to form a rather broad band of resonant states filling most of the bulk gap and merging with the top of the valence band. This seems to point either to a Ruderman-Kittel-Kasuya-Yoshida (RKKY) or to a superexchange interaction mediated by *p* carriers as the most likely source of exchange coupling among the magnetic impurities [45]. Cr-doped Sb_2Te_3 is clearly quite different since the impurities do not seem to introduce free carriers. Therefore, this case appears to be the best candidate for the Van Vleck mechanism of magnetic order, as originally suggested in Ref. [4]. However, this conclusion has been challenged by a recent paper, reporting the results of first-principles calculations in Cr-doped Sb_2Te_3 [44]. This study indicates that magnetic order is present even in the absence of spin-orbit interaction, which is the driving mechanism of band inversion and a nontrivial gap in TIs, ultimately responsible for establishing a strong Van Vleck spin susceptibility. According to this study, the mechanism responsible for magnetic order is instead due to the presence of an induced FM spin polarization in the Sb monolayer containing the Cr dopant, transferred widely from the magnetic TM impurity to distant Sb atoms by the long-range resonant *p*-bonding network known to exist within the QLs of the chalcogenide host material. Although we have not carried out any specific study of the Cr-Cr exchange coupling, our results on the induced AFM spin polarization of the NN Te atoms and the FM spin polarization of the next-NN Sb atoms (see Table I) are consistent with the conclusion of Ref. [44].

Fe dopants are peculiar also when it comes to the possible source of magnetic order. As discussed above, the Fe impurity states present in the bulk gap appear to form a band of localized impurity *d* orbitals of minority-spin character. Note also that in the energy region of these states, there is no presence of *p* levels of the host material. On the basis of these results, we are led to conclude that magnetic order in Fe-doped Sb_2Te_3 should be quite weak, if present at all. Finally, Mn-doped Sb_2Te_3 closely resembles the dilute magnetic semiconductor (Ga,Mn)As, with a hole state of *p* character residing mostly on the NN atoms of the host, but hybridized with Mn *d* levels. Therefore, Mn-doped Sb_2Te_3 should be characterized by a carried-mediated RKKY exchange coupling. Note that, according to our calculations, Mn displays the largest magnetic moment of all four dopants. However, the presence of a large microscopic magnetic moment of the individual dopants does not guarantee the onset of a robust magnetic order, which also depends on the dopant concentration and on the degree of *p*-*d* hybridization.

III. CRYSTAL GROWTH

Magnetically doped Sb_2Te_3 samples were grown by vertical Bridgman crystallization in conically shaped carbon-coated quartz ampoules. Elementary Sb, Te, V, Cr, Mn, and Fe were weighed to obtain the chemical composition $Sb_{2-x}TM_xTe_3$. After sealing under a residual pressure of 1 mbar, the ampoules were horizontally soaked at 700 °C for several days to ensure that magnetic impurities were homogeneously distributed. Subsequently, the samples were subjected to Bridgman recrystallization under an axial temperature gradient of 15 °C/cm and ampoule translation rate of 10 mm/day [68].

IV. SCANNING TUNNELING MICROSCOPY AND SPECTROSCOPY

Systematic STM/STS measurements have been performed with the goal of obtaining detailed information on the impact that different doping elements have on both structural and electronic properties of the host material. In this context, the high spatial resolution of STM together with its capability of providing detailed spectroscopic information for energies close to the Fermi level makes it an ideal technique to visualize impurity-induced local changes in the density of states emerging within the Sb_2Te_3 bulk band gap.

Single crystals have been cleaved at room temperature in ultrahigh vacuum (UHV) and immediately inserted into the microscope operated at a temperature $T = 4.8$ K. All measurements have been performed using electrochemically etched tungsten tips. Spectroscopic data have been obtained using the lock-in technique by adding a bias voltage modulation in-between 1 and 10 meV (r.m.s.) at a frequency $f = 793$ Hz. Results for V, Cr, Mn, and Fe are reported in Figs. 5, 6, 7, and 8, respectively.

For all elements, topographic images reveal the presence of different defects in the crystals. The large overviews reported in

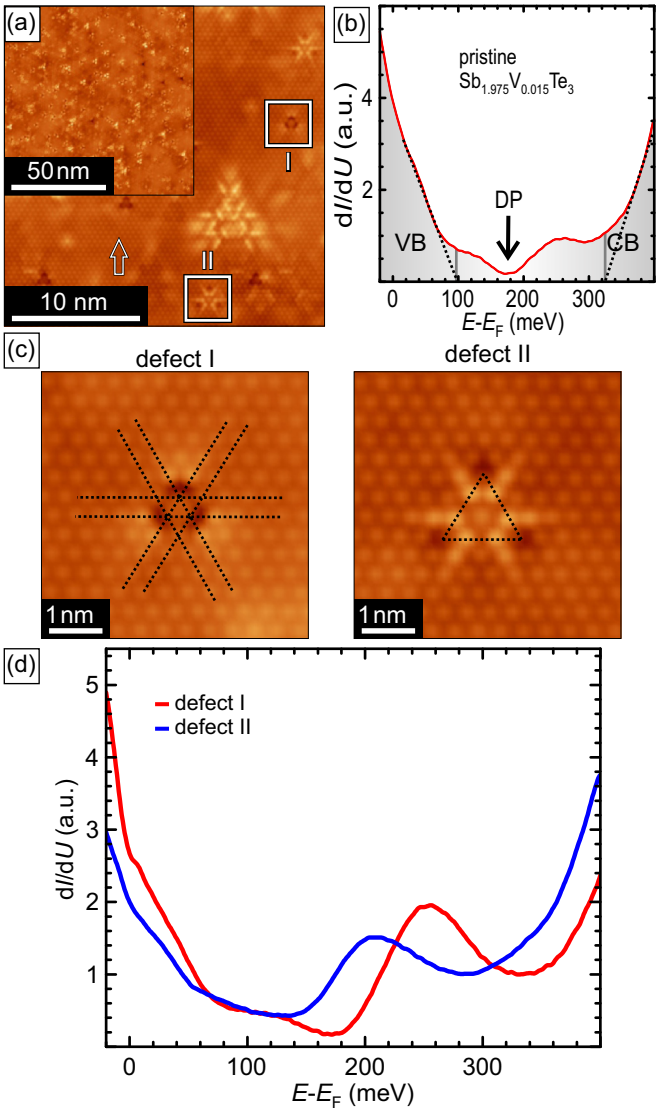

FIG. 5. Scanning tunneling microscopy and spectroscopy data obtained on V-doped Sb_2Te_3. The dopants' concentration amounts to 1.5% V in each Sb layer. (a) Topographic images reveal the existence of two different doping sites (see white boxes labeled I and II). (b) Local density of states acquired over a defect-free area [see arrow in (a)]. (c) Atomically resolved images allow to precisely identify defects I and II as V atoms substituting Sb in the second and fourth layers of the Te-Sb-Te-Sb-Te quintuple-layer structure, respectively. (d) Local density of states acquired by positioning the tip on top of the dopants.

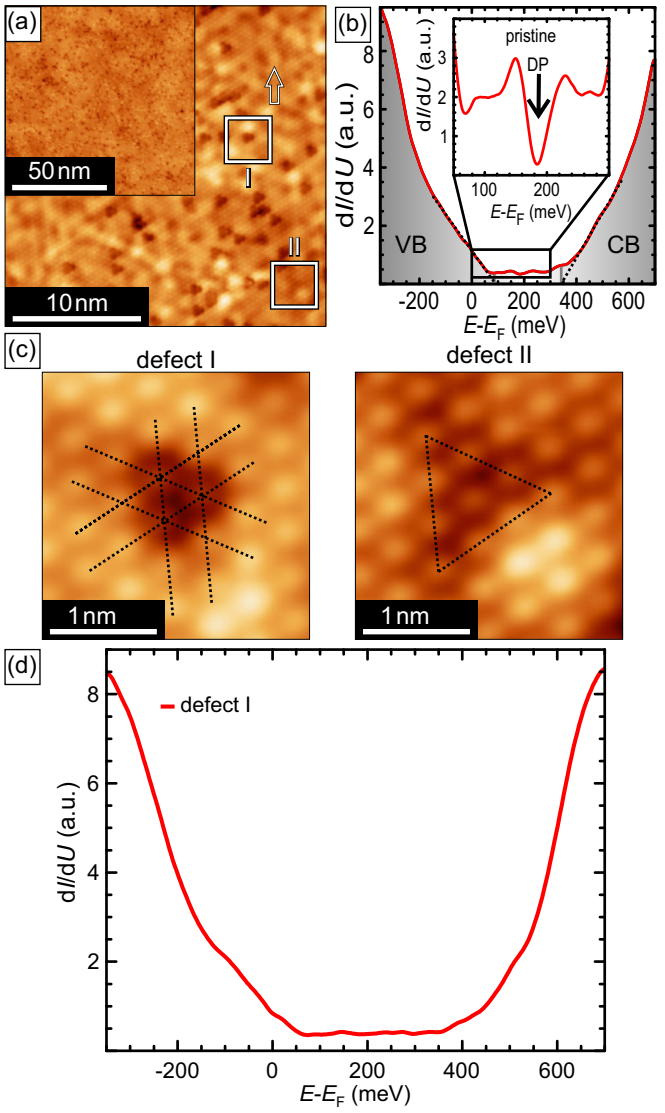

FIG. 6. Scanning tunneling microscopy and spectroscopy data obtained on Cr-doped Sb_2Te_3. The dopants' concentration amounts to 1.5% Cr in each Sb layer. (a) Topographic images reveal the existence of two different doping sites (see white boxes labeled I and II). (b) Local density of states acquired over a defect-free area [see arrow in (a)]. (c) Atomically resolved images allow to precisely identify defects I and II as Cr atoms substituting Sb in the second and fourth layers of the Te-Sb-Te-Sb-Te quintuple-layer structure, respectively. (d) Local density of states acquired by positioning the tip on top of defect I. The spectrum strongly resembles the one obtained over a defects-free area. In particular, not any new state emerges within the bulk gap. The perturbation introduced in the surface density of states by defect II is vanishingly small and its STS spectrum can not be disentangled from the one obtained over defects-free areas.

panels (a) of Figs. 5–8 as insets demonstrate that in all crystals the magnetic dopants are homogeneously distributed, without any signature of clustering. Furthermore, irrespective of the particular TM dopant, two types of defects, labeled I and II, are predominant. These defects correspond to the perturbations introduced in the crystal structure by the magnetic dopants, which are expected to substitute Sb in the second and fourth layers of the Te-Sb-Te-Sb-Te quintuple layer structure [16]. Although Sb substitution is energetically most favorable, interstitial doping has also been reported [33]. This necessarily calls for a precise identification of the dopants' sites. Indeed, the different local environment seen by impurities residing at different sites can significantly change the impurity-host hybridization, ultimately impacting onto the system's electronic and magnetic properties. As discussed in Refs. [69,70], this information can be obtained by analyzing both the symmetry as well as the spatial extension of the dopant-induced defects with respect to the atomically resolved periodicity of the surface. As shown in panels (c) of Figs. 5–8, this method allows us to identify defects I and II as magnetic atoms substituting Sb in the

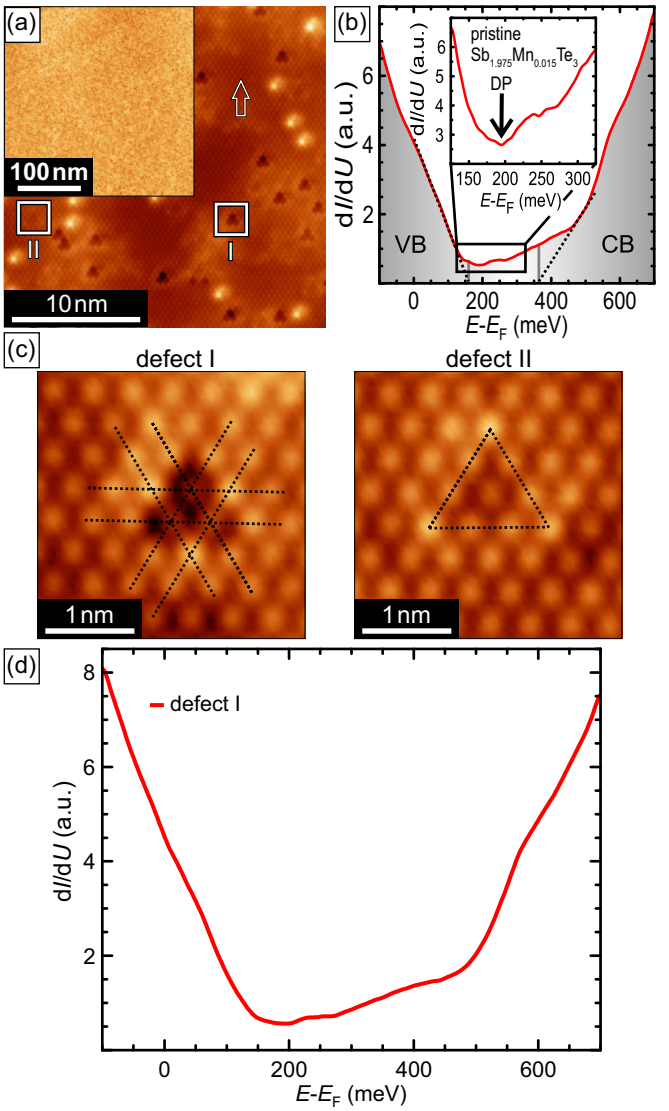

FIG. 7. Scanning tunneling microscopy and spectroscopy data obtained on Mn-doped Sb_2Te_3. The dopants' concentration amounts to 1.5% Mn in each Sb layer. (a) Topographic images reveal the existence of two different doping sites (see white boxes labeled I and II). (b) Local density of states acquired over a defect-free area [see arrow in (a)]. (c) Atomically resolved images allow to precisely identify defects I and II as Mn atoms substituting Sb in the second and fourth layers of the Te-Sb-Te-Sb-Te quintuple-layer structure, respectively. (d) Local density of states acquired by positioning the tip on top of defect I. The spectrum strongly resembles the one obtained over a defects-free area. In particular, not any new state emerges within the bulk gap. The perturbation introduced in the surface density of states by defect II is vanishingly small and its STS spectrum can not be disentangled from the one obtained over defects-free areas.

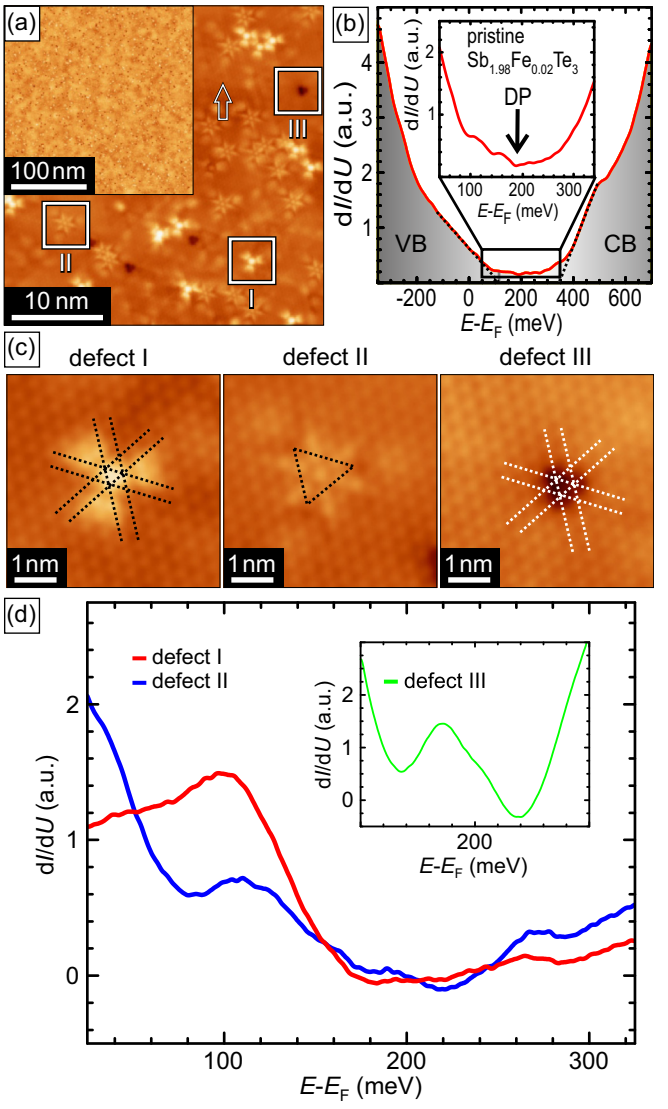

FIG. 8. Scanning tunneling microscopy and spectroscopy data obtained on Fe-doped Sb_2Te_3. The dopants' concentration amounts to 0.5% Fe in each Sb layer. (a) Topographic images reveal the existence of two predominant doping sites (see white boxes labeled I and II). An additional but less frequently observed appearance is also found (see III). (b) Local density of states acquired over a defect-free area [see arrow in (a)]. (c) Atomically resolved images allow to precisely identify defects I and II as Fe atoms substituting Sb in the second and fourth layers of the Te-Sb-Te-Sb-Te quintuple-layer structure, respectively. Defect III is structurally equivalent to I but characterized by a different contrast. (d) Local density of states acquired by positioning the tip on top of the dopants.

second and fourth layers of the Te-Sb-Te-Sb-Te quintuple-layer structure, respectively.

The structural investigation already allows us to evidence some differences and similarities among the different impurities. The cleavage planes of V- and Fe-doped samples have a quite similar appearance: dopants residing in the topmost Sb layer (defect I) are characterized by a triangular depression with brighter intensity at each corner. We would like to note that in the Fe case an additional but less frequently observed appearance is found for dopants residing in the first Sb layer [defect III in Fig. 8(c)]. This site is structurally equivalent to I but characterized by a different contrast. Although a definitive conclusion can not be drawn at the moment, we speculate that defect III might be related to Fe atoms in a different oxidation state [71]. Dopants substituting the second Sb layer (defect II) appear as starlike features. This scenario is different with respect to the one observed in Cr- and Mn-doped samples, where triangular depressions are visible for both doping sites.

Since all magnetic TM elements are occupying the very same crystal site, they are always perturbing the very same bonds. The different appearance visible on the surface is thus a direct signature of a TM-dependent impurity-host hybridization. Along this line, strong similarities are also expected to manifest in the electronic structures, with V- and Fe-doped samples on one side and Cr- and Mn-doped samples on the other side.

Electronic aspects have been investigated by analyzing the local density of states as inferred by STS measurements. Panels (b) of Figs. 5–8 show the results obtained by positioning the tip away from any defects [see arrows in panels (a)]. As described in Refs. [16,72], the minimum visible in the spectra marks the position of the Dirac point. The sharp conductance increases above and below the Dirac point can be used to map the position of valence band maximum and conduction band minimum. Their difference results in a bulk gap of approximately 175 meV, in good agreement with previous reports [16,69,72].

The impact of the dopants onto the sample electronic properties has been analyzed by acquiring STS spectra with the tip positioned directly on top of the two different magnetic dopants (I and II). For both V and Fe, these spectra [reported in panels (d) of Figs. 5–8] highlight the emergence of broad resonances residing within the bulk gap at energies close to the Dirac point. Quite contrary, data acquired over Cr and Mn dopants do not evidence any additional feature, as these spectra are virtually identical to those obtained in defects-free samples areas. These experimental observations are in agreement with the theoretical calculations presented in Sec. II B 3 which showed that V and Fe atoms generate a substantial impurity-induced spectral weight at the Dirac point, whereas Cr and Mn leave the Dirac node almost unaffected (see Fig. 4). Overall, these findings indicate that magnetic impurities can profoundly alter the density of states within the bulk gap, making the observation of a magnetic-induced opening in the surface Dirac cone impossible. This is not only the case in V- and Fe-doped samples, where strong impurity resonances can effectively fill the magnetic gap. Indeed, although being strongly suppressed, a nonvanishing contribution to the total density of states is present also for Cr and Mn. This is clearly evidenced by the Cr-doped sample where, despite the presence of long-range ferromagnetic order (see XMCD data and related discussion), the surface remains gapless as highlighted by the zoomed STS spectrum [see Fig. 6(b): the differential conductivity never goes to zero but simply reaches a minimum].

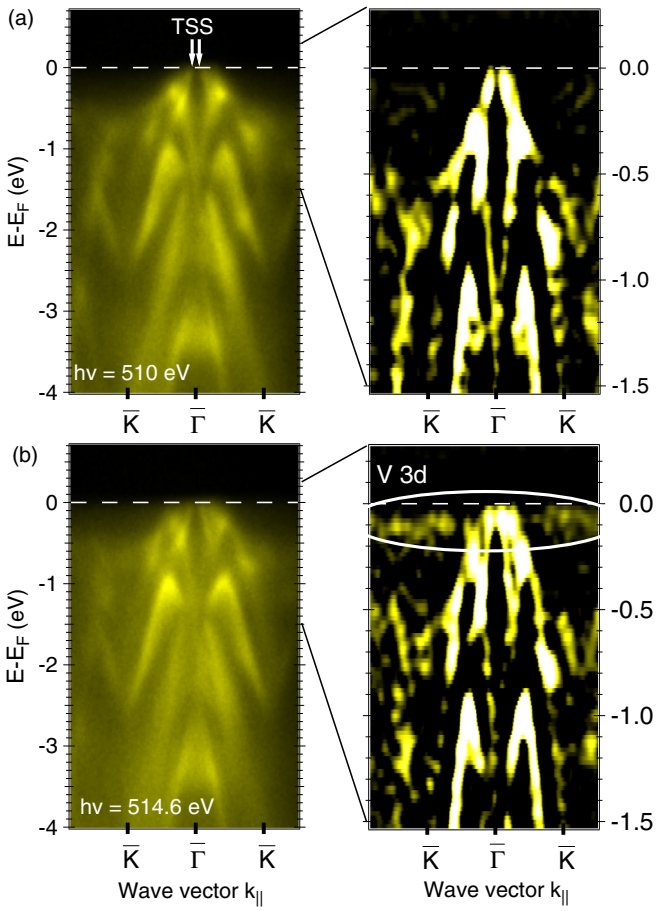

FIG. 9. Angle-resolved resonant photoemission data for V-doped Sb_2Te_3. On- and off-resonant data sets, as well as corresponding second-derivative images, are shown in (a) and (b), respectively [cf. Fig. 10(a) for the corresponding L_3 XAS spectrum]. Despite the strong p doping of Sb_2Te_3, the tails of the topological surface state (TSS) extending into the valence band are observed [73]. In the on-resonant data in (b), a dispersionless feature is observed near the Fermi level, which is attributed to a V 3d impurity band [11].

V. RESONANT PHOTOEMISSION MEASUREMENTS

In this section we shall discuss resonant photoemission data that were obtained for the same V-, Cr-, Mn-, and Fe-doped Sb_2Te_3 samples studied by STM/STS in the previous section. This method provides a rather direct estimate of the 3d impurity DOS in the valence band by exploiting their strongly enhanced photoemission cross section for excitation energies close to the 2p-3d x-ray absorption (XAS) maximum [74,75]. Typically, this is achieved by considering the difference between an "on-resonant" spectrum, obtained at the XAS maximum, and an "off-resonant" spectrum, obtained at an energy just below the XAS threshold. The results can be directly compared to the calculated DOS in Sec. II, thus complementing the STS data which cannot access electronic states residing well below the Fermi level.

The resonant photoemission data were obtained at beamline P04 of the PETRA III storage ring at DESY (Germany) using the ASPHERE III setup designed for soft x-ray photoemission experiments. The measurements were performed with a Scienta R4000 spectrometer at a base pressure of about 3×10^{-10} mbar and a temperature of about 30 K. The energy resolution was about 100 meV and for all measurements circularly polarized light has been used.

Figures 9(a) and 9(b) display angle-resolved off- and on-resonant photoemission data for V-doped Sb_2Te_3 showing well-defined band dispersions. Due to the strong intrinsic p-type doping, the Dirac point of the topological surface state (TSS) lies above the Fermi level and, hence, is inaccessible to photoemission. This is in agreement with our STS results in Fig. 2. However, the high-binding-energy tails of the TSS extend into the valence band up to a binding energy of about 0.3 eV, as shown previously for undoped Sb_2Te_3 by high-resolution ARPES [73]. Remarkably, the TSS can also be

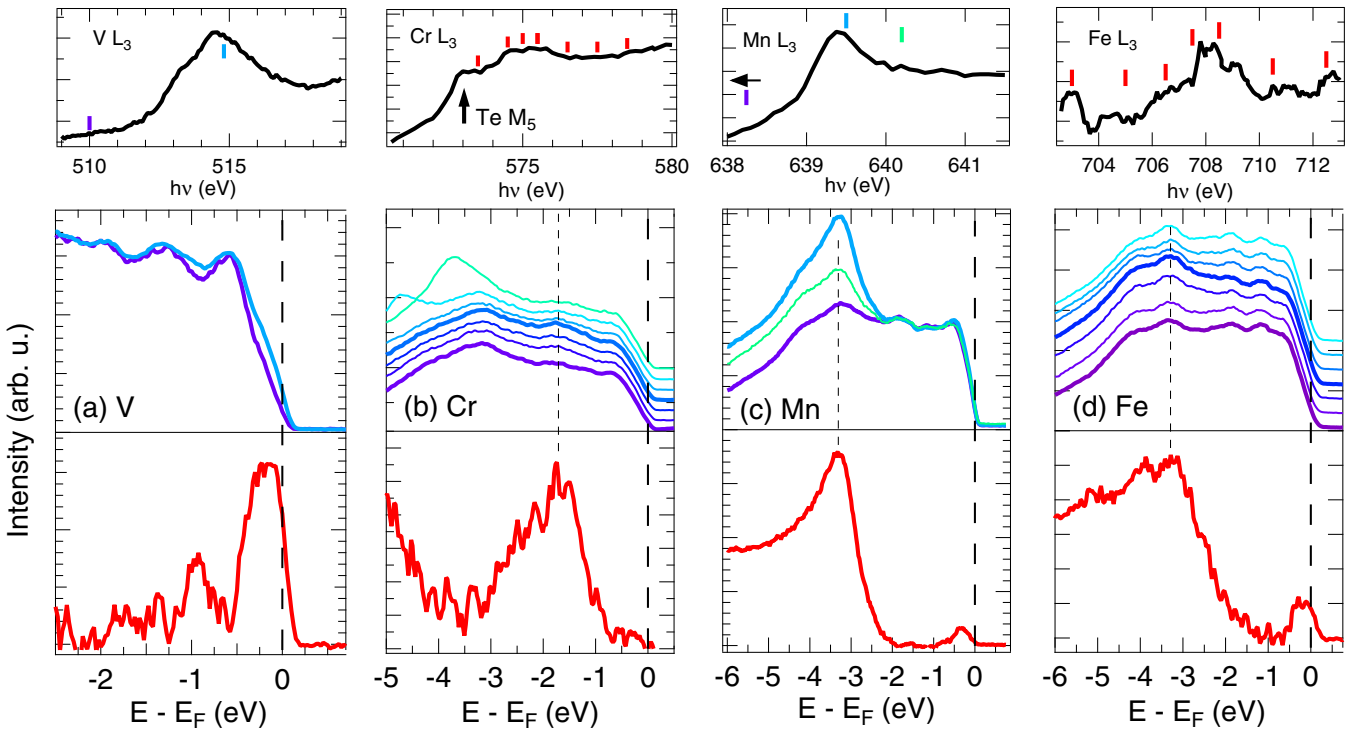

FIG. 10. Resonant photoemission data for (a) V-, (b) Cr-, (c) Mn-, and (d) Fe-doped Sb_2Te_3. The top panels show the respective $2p$-$3d$ L_3 absorption edges. The markers indicate the photon energies $h\nu$ used for the resonant photoemission measurements shown in the middle panels. The photoemission spectra in (b) and (d) are offset, with the bottom (top) spectrum corresponding to the lowest (highest) photon energy. The off-resonant spectrum in (c) was acquired at $h\nu = 635$ eV, as indicated by the arrow. The pronounced features at higher binding energy in the two topmost spectra in (b) are artifacts arising from the second harmonic of the beamline and the energetic overlap between the Cr $2p$ and Te $3d$ core levels (see XAS spectrum). The bottom panels show the difference between an on-resonant and an off-resonant spectrum, which are indicated by thick lines in the middle panels. The difference spectra provide an estimate of the $3d$ impurity DOS that can be compared to the corresponding theoretical calculations in Fig. 2.

discerned in the present soft x-ray ARPES data, as indicated in Fig. 9(a).

In order to address the V $3d$ states, we consider the second-derivative images in Figs. 9(a) and 9(b) (right panels), that were obtained from the raw-data sets (left panels). In the on-resonant image one can discern a weak, dispersionless feature near the Fermi level that is absent in the off-resonant image and, hence, is attributed to a V $3d$ impurity band. The presence of V states near the Fermi level is further demonstrated by the angle-integrated data in Fig. 10(a). The on-resonant spectrum shows a shoulder at a binding energy of about 0.15 eV, leading to a line-shape deviation from the off-resonant spectrum. The resulting difference spectrum indicates a metallic V $3d$ DOS extending down to a binding energy of about 0.5 eV. This observation is in good agreement with our theoretical calculation of the V DOS shown in Fig. 2 and with previous measurements for V-doped $(BiSb)_2Te_3$ thin films [11]. In particular, the direct comparison appears to favor the calculation without an additional onsite interaction parameter U, possibly indicating a minor role of correlation effects. Interestingly, our photoemission data demonstrate an energy overlap of V impurity states and the TSS, facilitating an interaction between them, as observed in our STS experiments in Sec. IV and in previous reports [16].

Resonant photoemission data for Cr-doped Sb_2Te_3 are displayed in Fig. 10(b). The photon energy-dependent spectra across the Cr L_3 edge show a resonating feature at a binding energy of about 1.7 eV. Accordingly, the difference spectrum indicates a maximum in the Cr $3d$ DOS at this energy. This finding is in good agreement with our theoretical results for Cr reported in Fig. 2.

Figure 10(c) shows resonant photoemission data for Mn-doped Sb_2Te_3. We find a pronounced Mn $3d$ feature at a binding energy of about 3.3 eV. Furthermore, an additional hump centered at about 0.3 eV binding energy leads to a finite DOS at the Fermi level. These observations are in good agreement with our calculations (see Fig. 2). Similar features in the Mn DOS have also been found for (Ga,Mn)As [75].

The resonant photoemission data for Fe-doped Sb_2Te_3 reported in Fig. 10(d) show a main peak centered at a binding energy slightly below 3.0 eV. This is in line with our theoretical predictions which evidence a maximum in the Fe $3d$ majority states at similar energies (see Fig. 2). The experimental data also suggest the presence of Fe states near the Fermi level, which our calculations can directly link to the presence of a metallic $3d$ minority band.

VI. XMCD MEASUREMENTS

To probe the magnetic properties of the TM dopants embedded in the TI host, XMCD measurements were performed at the BOREAS beamline of the ALBA synchrotron light source [76] and at the ID32 beamline of the European Synchrotron Radiation Facility [77]. The samples were cleaved *in situ*

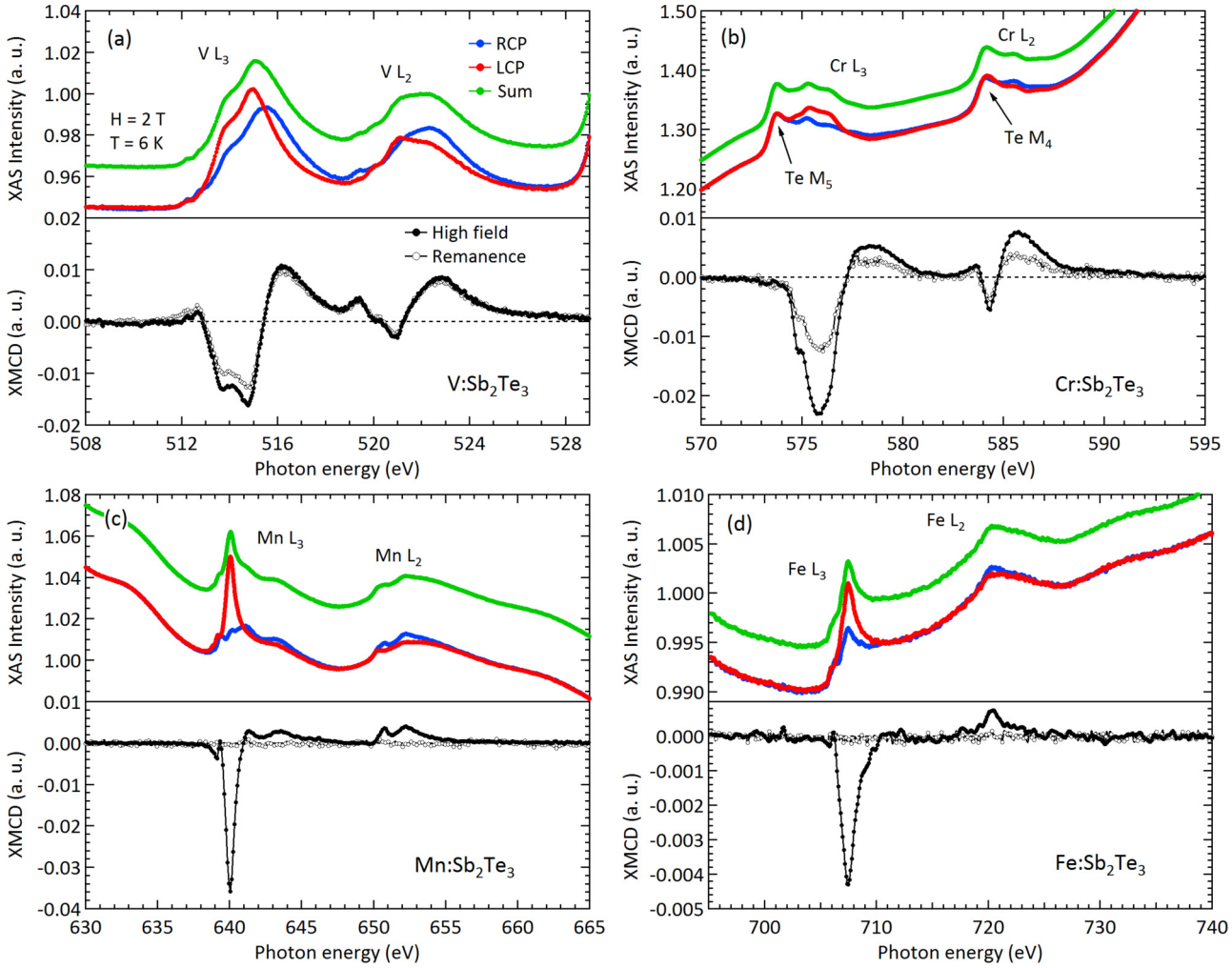

FIG. 11. X-ray absorption (XAS) and magnetic dichroism (XMCD) spectra at the $L_{2,3}$ edges ($2p$-$3d$ transition) of the TM element from (a) V-, (b) Cr-, (c) Mn-, and (d) Fe-doped Sb_2Te_3 single crystals. The XAS spectra for left (LCP) and right (RCP) circularly polarized light are shown in the upper panels (red and blue curves, respectively). The corresponding XMCD spectra, defined as $(R - L)/(R + L)$, are shown as the black curves in the lower panels, and reveal a sizable localized magnetic moment carried by the $3d$ states.

under UHV conditions. The experiments were carried out at temperatures $T < 10$ K in the total electron yield mode, which makes our measurements mostly surface sensitive. In Fig. 11 we plot the L-edge absorption spectra for left and right circularly polarized light (red and blue curves, respectively) and their corresponding XMCD spectra (black curves) for each of the Sb_2Te_3 systems doped with (a) V, (b) Cr, (c) Mn, and (d) Fe, measured under a magnetic field applied along the surface normal. The strong contribution of the background in the XAS line shapes is related to the low concentration of the dopants. The Sb_2Te_3 single crystals exhibited slightly different dopant concentrations, namely, 1.5% V, 1.5% Cr, 1.5% Mn, and 0.5% Fe in each Sb layer. Despite the complex multiplet fine structure of the TM L edges and the clear overlap between the Cr L and Te M edges, no sign of contaminated (oxidized) TM species was observed in the system. A clear XMCD signal is detected in all our samples, proving that V, Cr, Mn, and Fe dopants carry a net magnetic moment once embedded into Sb_2Te_3. Our results for V- and Cr-doped Sb_2Te_3 qualitatively reproduce previous XMCD studies [16,27] whereas no similar study has been found for the Mn- and Fe-doped systems.

Although doping with V, Cr, Mn, and Fe always results in the introduction of magnetic moments into the system, the long-range magnetic properties can be strongly TM dependent. This is expected because of the element-specific p-d hybridization between dopant and host material, which plays a crucial role in mediating the coupling between magnetic moments in TM-doped TIs.

These aspects have been investigated by measuring hysteresis loops at the L_3 XMCD maximum, for a magnetic field applied at different angles θ with respect to the surface normal. The systems studied here showed very different macroscopic magnetic behaviors. In Fig. 12 we show the resulting magnetization curves for $\theta = 0^\circ$ (full circles) and $\theta = 60^\circ$ (hollow circles) for (a) V-, (b) Cr-, (c) Mn-, and (d) Fe-doped systems. For the V- and Cr-doped samples, a ferromagnetic hysteresis curve can be seen, showing a clear trend towards an out-of-plane ground-state magnetization. In particular, the V-doped sample exhibits an opening of the hysteresis loop, with a coercivity of approximately 150 mT, as seen in the inset in Fig. 12(a). For Cr, a collective ferromagnetic response is highlighted by the steplike behavior

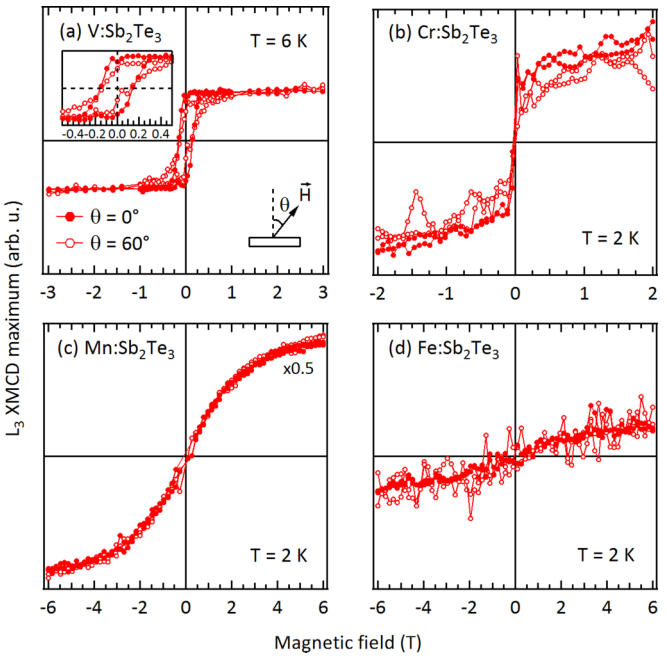

FIG. 12. Hysteresis loops taken at the L_3 XMCD maximum of each TM element for (a) V-, (b) Cr-, (c) Mn-, and (d) Fe-doped Sb_2Te_3 single crystals for magnetic field applied at angles $\theta = 0°$ (full circles) and $\theta = 60°$ (hollow circles) with respect to the surface normal. V- and Fe-doped samples show a paramagnetic response at these low concentrations (see text), whereas the Mn-doped samples are rather isotropic and Cr-doped samples tend to favor an out-of-plane easy axis, as expected for QAH systems. The different macroscopic magnetic properties are determined by the doping concentration and the strength of the *p-d* hybridization between the impurity and host states, which ultimately determine the dominant magnetic interactions in the system.

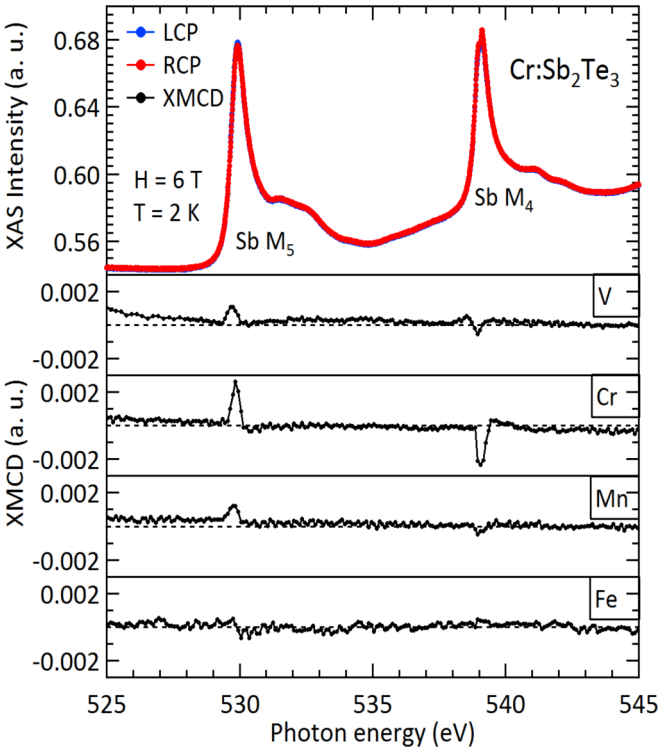

FIG. 13. XAS and XMCD spectra at the Sb $M_{4,5}$ edges ($3d$-$5p$ transition). Upmost panel: XAS line shape for incident left (blue) and right (red) circularly polarized light, from a Cr-doped Sb_2Te_3 sample. Lower panels: corresponding XMCD spectra (black curves). The XMCD signal seen at the Sb M edges is attributed to a partial spin polarization of the Sb p states at the valence band via p-d hybridization with the impurity states of the neighboring TM ions.

of the hysteresis curve. However, the coercivity in this case could not be measured, being it smaller than the resolution of our measurements. The Mn-doped sample showed the largest XMCD signal, which is indicative of a high-spin configuration of the dopants. However, long-range magnetic order is absent in this system: the hysteresis loops show no sign of saturation up to a field of 6 T. Furthermore, data taken along normal and grazing magnetic field directions are indistinguishable, indicating the absence of any detectable preferred magnetization direction. Finally, the Fe-doped sample showed a paramagnetic behavior. The low concentration results in a small signal which makes it difficult to draw definitive conclusions over the magnetic easy axis.

On the basis of the results of our theoretical studies (see also the discussion in the last two paragraphs at the end of Sec. II B 4), it seems that V and Mn are the only two cases where a RKKY type of interaction could be the origin of FM order. The hysteresis results presented here suggest that in the case of V, the carrier concentration provided by the dopants might be enough to establish a FM ground state. In the case of Mn, the observation of a very weak magnetic signal leads us to exclude the presence of a robust FM state. In this case, other types of disordered magnetic states, possibly related to spin-glass states, can occur.

As previously discussed, the magnetic impurities are expected to induce a magnetic moment in the neighboring Te and Sb atoms via p-d hybridization. This has been directly detected by XMCD measurements. Figure 13 (upmost panel) shows an example of the Sb $M_{4,5}$-edge line shapes for left and right circularly polarized light (blue and red curves, respectively), measured at a Cr-doped sample. They show no sign of oxygen contamination (O K edge lies at 535 eV) and are highly reproducible in all samples. The lower panels show the Sb $M_{4,5}$ XMCD spectra for samples doped with the different transition metals, as labeled in the figure. The intensity of this signal depends on the dopant concentration and the degree of p-d hybridization. In V, Cr, and Mn-doped samples, our measurements reveal a small magnetic dichroism at the Sb $M_{4,5}$ edge. The XMCD signal has an opposite sign as compared to the corresponding TM L edges. This proves the existence of ferromagnetic coupling between TM and Sb ions. All these observations are in agreement with our theoretical predictions. The Fe case could not be experimentally scrutinized. The magnetic polarization of Sb induced by Fe, if any, is below our detection limit due to the three times lower amount of Fe in the sample, as compared to the other $3d$ elements.

Finally, we would like to compare the experimental and theoretical magnetic anisotropy directions. For Cr-doped Sb_2Te_3, our calculations predict an out-of-plane easy axis for both surface and bulk dopants, perfectly in line with the

experimental results. On the other hand, for V-doped samples our calculations predict a strong in-plane anisotropy at the surface and a weak out-of-plane anisotropy in the bulk. This seemingly apparent discrepancy between theory and experiments can be explained by considering the XAS/XMCD probing depth. Indeed, although being very surface sensitive, our measurements do not exclusively access the very top layer but probe the sample up to a thickness of a few nanometers. Furthermore, the presence of bulk long-range ferromagnetic order can effectively act onto the surface magnetic moments, forcing them to align along the surface normal. This observation also explains the experimental data obtained on Mn-doped samples. According to our calculations, Mn surface and bulk impurities are predicted to have in-plane and out-of-plane easy axis, respectively, with the strength of the magnetic anisotropy energy being roughly the same for the two cases. Summing these two contributions results in the absence of any preferred direction, in agreement with our experimental evidence. In conclusion, we can say the experimental results for the magnetic anisotropy axis are consistent with the results of the theoretical calculations for those cases, like Cr, where theory predicts the same easy axis for both bulk and surface doping. For the impurities where theory and experiment do not agree, such as V, the discrepancy is most likely due to the fact that our surface calculations are done by substituting a Sb atom by an impurity only at the topmost Sb layer. Therefore, the effect of bulk magnetic order on the surface properties is not accounted for in the surface calculations. In the experiment, however, impurities are distributed throughout the entire sample. Therefore, the presence of bulk magnetic order, interplaying and possibly competing with surface effects like in the case of V, can influence the easy axis of system. Note that V and Mn are the two cases for which our calculations predict that bulk anisotropy and surface anisotropy (see Table II) have opposite easy axis. For this situation, the final outcome of the overall anisotropy might depend on details which are difficult to disentangle theoretically.

VII. CONCLUSIONS

In this work we have investigated the electronic and magnetic properties of Sb_2Te_3 doped with different substitutional transition metal impurities (namely, V, Cr, Mn, Fe). Our calculations show that magnetic impurities induce spin polarization at the host atoms. Both in bulk and in surface doping V, Cr, and Mn couple antiferromagnetically with the NN Te atoms, while Fe couples ferromagnetically. In all cases, the impurity atom couples ferromagnetically with NN Sb host atoms.

The magnetic anisotropy of TM doped Sb_2Te_3 depends not only on the type of TM impurity, but also on its position. Specifically, the theoretical results have shown that while the easy axis for V and Mn is out of plane for bulk impurities, it becomes in plane for surface impurities. For Cr doping the easy axis is along the out-of-plane direction for both bulk and surface doping. Fe is the only impurity displaying an in-plane anisotropy for both bulk and surface doping.

One of the important conclusions of this work is that substitutional magnetic TM impurities do not necessarily open a gap at the DP. This apparent contradiction is effectively explained by the possible presence of impurity resonances. Specifically, in the case of V and Fe, we find that impurity states appear to significantly contribute to the density of states at energies close to the DP.

These theoretical predictions have been compared with experimental results. In agreement with DFT calculations, STS data revealed that both V and Fe dopants introduce strong impurity states within the bulk gap, whereas no resonances are detected for Cr and Mn. The use of resPES allowed us to directly access the $3d$ character of the impurity states, further corroborating the validity of our calculations. Finally, the magnetic properties have been experimentally scrutinized by XMCD measurements. All dopants have been found to induce a magnetic moment in the Sb atoms, signaling the p-d hybridization taking place between impurities and host material. On the other hand, long-range magnetic order is established only for V- and Cr-doped samples.

The results of the present joint theoretical and experimental study have implications for the understanding of the microscopic nature of the QAHE in magnetically doped TIs, and provide indications of the most promising systems that could display enhanced forms of QAHE. One conclusion of our work is that, for the same host material Sb_2Te_3, the compliance of the canonical conditions for the realization of the QAHE, i.e., robust long-range ferromagnetic order with out-of-plane anisotropy and absence of bulk conducting states in the vicinity of the Dirac point, depends crucially on the nature of the doping. For this reason, Mn and Fe are not expected to satisfy the conditions for the onset of the QAHE, mainly due to the lack of a robust ferromagnetic order. Of the other two impurities, Cr is the most clear-cut system to host a robust QAHE: it displays a reasonably strong out-of-plane ferromagnetic order (in this case, our theoretical results agree with experiment) and no extra states appear in the bulk gap as a result of doping. Our results for Cr are in agreement with a recent theoretical study [44], which for these reasons finds Cr-doped Sb_2Te_3 (and $BiSb_2Te_3$) to be the best candidate to host a robust QAHE and suggests ways to further enhance the temperature range where it can occur. V doping is perhaps the most interesting and challenging case of the four investigated. For this impurity, XMCD results indicate the presence of strong ferromagnetic order with an out-of-plane easy axis. On the other hand, the presence of impurity states in the bulk gap of TI in the vicinity of Dirac point is now confirmed by both experimental and theoretical studies and defies the second condition for the QAHE [16]. The observation of a clear QAHE for this system [9], essentially with the same degree of precision found in Cr-doped Sb_2Te_3, can possibly be explained by invoking the existence of a mobility gap, similar to the one responsible for the perfect Hall quantization in GaAlAs 2D electron gas systems. Given this more complex scenario, further rational quantum engineering and material optimization of V-doped Sb_2Te_3 TI, for example by codoping, in order to enhance its QAHE properties, is probably more challenging than for Cr-doped TIs.

ACKNOWLEDGMENTS

This work was supported by the Faculty of Technology and by the Department of Physics and Electrical Engineering at Linnaeus University (Sweden). C.M.C. and M.F.I.

acknowledge financial support from the Swedish Research Council (VR) through Grant No. 621-2014-4785, and by the Carl Tryggers Stiftelse through Grant No. CTS 14:178. Computational resources have been provided by the Lunarc Center for Scientific and Technical Computing at Lund University. The XAS and XMCD experiments were performed at the BOREAS beamline at ALBA Synchrotron and at the ID32 beamline of the European Synchrotron Radiation Facility. O.E.T. and K.A.K. have been supported by the Russian Science Foundation (Project No. 17-12-01047). This work was supported by the DFG through SFB1170 "ToCoTronics" (projects A01 and A02).

[1] M. Z. Hasan and C. L. Kane, Rev. Mod. Phys. **82**, 3045 (2010).
[2] X.-L. Qi and S.-C. Zhang, Rev. Mod. Phys. **83**, 1057 (2011).
[3] F. D. M. Haldane, Phys. Rev. Lett. **61**, 2015 (1988).
[4] R. Yu, W. Zhang, H.-J. Zhang, S.-C. Zhang, X. Dai, and Z. Fang, Science **329**, 61 (2010).
[5] Q. Liu, C.-X. Liu, C. Xu, X.-L. Qi, and S.-C. Zhang, Phys. Rev. Lett. **102**, 156603 (2009).
[6] J. Henk, M. Flieger, I. V. Maznichenko, I. Mertig, A. Ernst, S. V. Eremeev, and E. V. Chulkov, Phys. Rev. Lett. **109**, 076801 (2012).
[7] C.-Z. Chang, J. Zhang, X. Feng, J. Shen, Z. Zhang, M. Guo, K. Li, Y. Ou, P. Wei, L.-L. Wang *et al.*, Science **340**, 167 (2013).
[8] C. Chang and M. Li, J. Phys.: Condens. Matter **28**, 123002 (2016).
[9] C.-Z. K-Chang, W. Zhao, D. Y. Kim, H. Zhang, B. A. Assaf, D. Heiman, S.-C. Zhang, C. Liu, M. H. W. Chan, and J. S. Moodera, Nat. Mater. **14**, 473 (2015).
[10] C.-Z. Chang, W. Zhao, J. Li, J. K. Jain, C. Liu, J. S. Moodera, and M. H. W. Chan, Phys. Rev. Lett. **117**, 126802 (2016).
[11] T. R. F. Peixoto, H. Bentmann, S. Schreyeck, M. Winnerlein, C. Seibel, H. Maaß, M. Al-Baidhani, K. Treiber, S. Schatz, S. Grauer *et al.*, Phys. Rev. B **94**, 195140 (2016).
[12] A. Pertsova, C. M. Canali, and A. H. MacDonald, Phys. Rev. B **94**, 121409 (2016).
[13] J. Checkelsky, R. Yoshimi, A. Tsukazaki, K. S. Takahashi, Y. Kozuka, J. Falson, M. Kawasaki, and Y. Tokura, Nat. Phys. **10**, 731 (2014).
[14] A. J. Bestwick, E. J. Fox, X. Kou, L. Pan, K. L. Wang, and D. Goldhaber-Gordon, Phys. Rev. Lett. **114**, 187201 (2015).
[15] C.-Z. Chang, W. Zhao, D. Y. Kim, P. Wei, J. K. Jain, C. Liu, M. H. W. Chan, and J. S. Moodera, Phys. Rev. Lett. **115**, 057206 (2015).
[16] P. Sessi, R. R. Biswas, T. Bathon, O. Storz, S. Wilfert, A. Barla, K. A. Kokh, O. E. Tereshchenko, K. Fauth, M. Bode, and A. V. Balatsky, Nat. Commun. **7**, 12027 (2016).
[17] H. J. von Bardeleben, J. L. Cantin, D. M. Zhang, A. Richardella, D. W. Rench, N. Samarth, and J. A. Borchers, Phys. Rev. B **88**, 075149 (2013).
[18] L. J. Collins-McIntyre, M. D. Watson, A. A. Baker, S. L. Zhang, A. I. Coldea, S. E. Harrison, A. Pushp, A. J. Kellock, S. S. P. Parkin, G. van der Laan, and T. Hesjedal, AIP Advances **4**, 127136 (2014).
[19] W. Liu, D. West, L. He, Y. Xu, J. Liu, K. Wang, Y. Wang, G. van der Laan, R. Zhang, S. Zhang, and K. L. Wang, ACS Nano **9**, 10237 (2015).
[20] A. I. Figueroa, G. van der Laan, L. J. Collins-McIntyre, G. Cibin, A. J. Dent, and T. Hesjedal, J. Phys. Chem. C **119**, 17344 (2015).
[21] J. Ružička, O. Caha, V. Holý, H. Steiner, V. Volobuiev, A. Ney, G. Bauer, T. Duchoň, K. Veltruská, I. Khalakhan *et al.*, New J. Phys. **17**, 013028 (2015).
[22] M. R. Scholz, J. Sánchez-Barriga, D. Marchenko, A. Varykhalov, A. Volykhov, L. V. Yashina, and O. Rader, Phys. Rev. Lett. **108**, 256810 (2012).
[23] M. Li, C.-Z. Chang, B. J. Kirby, M. E. Jamer, W. Cui, L. Wu, P. Wei, Y. Zhu, D. Heiman, J. Li, and J. S. Moodera, Phys. Rev. Lett. **115**, 087201 (2015).
[24] J. Zhang, C.-Z. Chang, P. Tang, Z. Zhang, X. Feng, K. Li, L.-l. Wang, X. Chen, C. Liu, W. Duan *et al.*, Science **339**, 1582 (2013).
[25] X. Wei, J. Zhang, B. Zhao, Y. Zhu, and Z. Yang, Phys. Lett. A **379**, 417 (2015).
[26] M. Ye, K. Kuroda, Y. Takeda, Y. Saitoh, K. Okamoto, S.-Y. Zhu, K. Shirai, K. Miyamoto, M. Arita, M. Nakatake *et al.*, J. Phys.: Condens. Matter **25**, 232201 (2013).
[27] M. Ye, W. Li, S. Zhu, Y. Takeda, Y. Saitoh, J. Wang, H. Pan, M. Nurmamat, K. Sumida, F. Ji *et al.*, Nat. Commun. **6**, 8913 (2015).
[28] L. B. Abdalla, L. Seixas, T. M. Schmidt, R. H. Miwa, and A. Fazzio, Phys. Rev. B **88**, 045312 (2013).
[29] H. Li, Y. R. Song, M.-Y. Yao, F. Zhu, C. Liu, C. L. Gao, J.-F. Jia, D. Qian, X. Yao, Y. J. Shi, and D. Wu, J. Appl. Phys. **113**, 043926 (2013).
[30] L. R. Shelford, T. Hesjedal, L. Collins-McIntyre, S. S. Dhesi, F. Maccherozzi, and G. van der Laan, Phys. Rev. B **86**, 081304 (2012).
[31] T. Schlenk, M. Bianchi, M. Koleini, A. Eich, O. Pietzsch, T. O. Wehling, T. Frauenheim, A. Balatsky, J.-L. Mi, B. B. Iversen *et al.*, Phys. Rev. Lett. **110**, 126804 (2013).
[32] M. R. Mahani, A. Pertsova, M. F. Islam, and C. M. Canali, Phys. Rev. B **90**, 195441 (2014).
[33] M. D. Watson, L. J. Collins-McIntyre, L. R. Shelford, A. I. Coldea, D. Prabhakaran, S. C. Speller, T. Mousavi, C. R. M. Grovenor, Z. Salman, S. R. Giblin *et al.*, New J. Phys. **15**, 103016 (2013).
[34] F. Yang, Y. R. Song, H. Li, K. F. Zhang, X. Yao, C. Liu, D. Qian, C. L. Gao, and J.-F. Jia, Phys. Rev. Lett. **111**, 176802 (2013).
[35] Y. Ni, Z. Zhang, I. C. Nlebedim, R. L. Hadimani, G. Tuttle, and D. C. Jiles, J. Appl. Phys. **117**, 17C748 (2015).
[36] T. M. Schmidt, R. H. Miwa, and A. Fazzio, Phys. Rev. B **84**, 245418 (2011).
[37] Y. Fan, P. Upadhyaya, X. Kou, M. Lang, S. Takei, Z. Wang, J. Tang, L. He, L.-T. Chang, M. Montazeri *et al.*, Nat. Mater. **13**, 699 (2014).
[38] T. Eelbo, M. Waśniowska, M. Sikora, M. Dobrzański, A. Kozłowski, A. Pulkin, G. Autès, I. Miotkowski, O. V. Yazyev, and R. Wiesendanger, Phys. Rev. B **89**, 104424 (2014).
[39] J. Honolka, A. A. Khajetoorians, V. Sessi, T. O. Wehling, S. Stepanow, J.-L. Mi, B. B. Iversen, T. Schlenk, J. Wiebe, N. B. Brookes *et al.*, Phys. Rev. Lett. **108**, 256811 (2012).

[40] Z. L. Li, J. H. Yang, G. H. Chen, M.-H. Whangbo, H. J. Xiang, and X. G. Gong, Phys. Rev. B **85**, 054426 (2012).

[41] A. Nunez and J. Fernandez-Rossier, Solid State Commun. **152**, 403 (2012).

[42] M.-T. Tran, H.-S. Nguyen, and D.-A. Le, Phys. Rev. B **93**, 155160 (2016).

[43] G. Rosenberg and M. Franz, Phys. Rev. B **85**, 195119 (2012).

[44] J. Kim, S.-H. Jhi, A. H. MacDonald, and R. Wu, Phys. Rev. B **96**, 140410 (2017).

[45] M. G. Vergniory, M. M. Otrokov, D. Thonig, M. Hoffmann, I. V. Maznichenko, M. Geilhufe, X. Zubizarreta, S. Ostanin, A. Marmodoro, J. Henk *et al.*, Phys. Rev. B **89**, 165202 (2014).

[46] Y. L. Chen, J.-H. Chu, J. G. Analytis, Z. K. Liu, K. Igarashi, H.-H. Kuo, X. L. Qi, S. K. Mo, R. G. Moore, D. H. Lu *et al.*, Science **329**, 659 (2010).

[47] S.-Y. Xu, M. Neupane, C. Liu, D. Zhang, A. Richardella, L. A. Wray, N. Alidoust, M. Leandersson, T. Balasubramanian, J. Sánchez-Barriga, O. Rader *et al.*, Nat. Phys. **8**, 616 (2012).

[48] T. Valla, Z.-H. Pan, D. Gardner, Y. S. Lee, and S. Chu, Phys. Rev. Lett. **108**, 117601 (2012).

[49] Y. S. Hor, P. Roushan, H. Beidenkopf, J. Seo, D. Qu, J. G. Checkelsky, L. A. Wray, D. Hsieh, Y. Xia, S.-Y. Xu *et al.*, Phys. Rev. B **81**, 195203 (2010).

[50] Y. Okada, C. Dhital, W. Zhou, E. D. Huemiller, H. Lin, S. Basak, A. Bansil, Y.-B. Huang, H. Ding, Z. Wang, S. D. Wilson, and V. Madhavan, Phys. Rev. Lett. **106**, 206805 (2011).

[51] P. Sessi, F. Reis, T. Bathon, K. A. Kokh, O. E. Tereshchenko, and M. Bode, Nat. Commun. **5**, 5349 (2014).

[52] Y. Xu, J. Chiu, L. Miao, H. He, Z. Alpichshev, A. Kapitulnik, R. R. Biswas, and L. A. Wray, Nat. Commun. **8**, 14081 (2017).

[53] R. R. Biswas and A. V. Balatsky, Phys. Rev. B **81**, 233405 (2010).

[54] A. M. Black-Schaffer, A. V. Balatsky, and J. Fransson, Phys. Rev. B **91**, 201411 (2015).

[55] M. Zhong, S. Li, H.-J. Duan, L.-B. Hu, M. Yang, and R.-Q. Wang, Sci. Rep. **7**, 3971 (2017).

[56] P. Blaha, K. Schwarz, G. K. H. Madsen, D. Kvasnicka, and J. Luitz, WIEN2K, An Augmented Plane Wave Plus Local Orbitals Program for Calculating Crystal properties, Vienna University of Technology, Austria, 2001.

[57] J. P. Perdew, K. Burke, and M. Ernzerhof, Phys. Rev. Lett. **77**, 3865 (1996).

[58] T. L. Anderson and H. B. Krause, Acta Crystallogr. Sect. B **30**, 1307 (1974).

[59] X. Wang, D.-S. Wang, R. Wu, and A. Freeman, J. Magn. Magn. Mater. **159**, 337 (1996).

[60] P. Mahadevan, A. Zunger, and D. D. Sarma, Phys. Rev. Lett. **93**, 177201 (2004).

[61] M. F. Islam and C. M. Canali, Phys. Rev. B **85**, 155306 (2012).

[62] B. Leedahl, D. W. Boukhvalov, E. Z. Kurmaev, A. Kukharenko, I. S. Zhidkov, N. V. Gavrilov, S. O. Cholakh, P. H. Le, C. W. Luo, and A. Moewes, Sci. Rep. **7**, 5758 (2017).

[63] A. A. Zyuzin and A. A. Burkov, Phys. Rev. B **83**, 195413 (2011).

[64] A. A. Zyuzin, M. D. Hook, and A. A. Burkov, Phys. Rev. B **83**, 245428 (2011).

[65] A. A. Taskin, H. F. Legg, F. Yang, S. Sasaki, Y. Kanai, K. Matsumoto, A. Rosch, and Y. Ando, Nat. Commun. **8**, 1340 (2017).

[66] L. B. Duffy, A. I. Figueroa, L. Gładczuk, N.-J. Steinke, K. Kummer, G. van der Laan, and T. Hesjedal, Phys. Rev. B **95**, 224422 (2017).

[67] A. Pertsova and C. M. Canali, New J. Phys. **16**, 063022 (2014).

[68] K. A. Kokh, S. V. Makarenko, V. A. Golyashov, O. A. Shegai, and O. E. Tereshchenko, CrystEngComm **16**, 581 (2014).

[69] Y. Jiang, Y. Y. Sun, M. Chen, Y. Wang, Z. Li, C. Song, K. He, L. Wang, X. Chen, Q.-K. Xue *et al.*, Phys. Rev. Lett. **108**, 066809 (2012).

[70] T. Bathon, S. Achilli, P. Sessi, V. A. Golyashov, K. A. Kokh, O. E. Tereshchenko, and M. Bode, Adv. Mater. **28**, 2183 (2016).

[71] J.-M. Zhang, W. Ming, Z. Huang, G.-B. Liu, X. Kou, Y. Fan, K. L. Wang, and Y. Yao, Phys. Rev. B **88**, 235131 (2013).

[72] P. Sessi, O. Storz, T. Bathon, S. Wilfert, K. A. Kokh, O. E. Tereshchenko, G. Bihlmayer, and M. Bode, Phys. Rev. B **93**, 035110 (2016).

[73] C. Seibel, H. Bentmann, J. Braun, J. Minár, H. Maaß, K. Sakamoto, M. Arita, K. Shimada, H. Ebert, and F. Reinert, Phys. Rev. Lett. **114**, 066802 (2015).

[74] M. Mulazzi, A. Chainani, N. Katayama, R. Eguchi, M. Matsunami, H. Ohashi, Y. Senba, M. Nohara, M. Uchida, H. Takagi, and S. Shin, Phys. Rev. B **82**, 075130 (2010).

[75] M. Kobayashi, I. Muneta, Y. Takeda, Y. Harada, A. Fujimori, J. Krempaský, T. Schmitt, S. Ohya, M. Tanaka, M. Oshima, and V. N. Strocov, Phys. Rev. B **89**, 205204 (2014).

[76] A. Barla, J. Nicolas, D. Cocco, S. M. Valvidares, J. Herrero-Martin, P. Gargiani, J. Moldes, C. Ruget, E. Pellegrin, and S. Ferrer, J. Synchrotron Radiat. **23**, 1507 (2016).

[77] K. Kummer, A. Fondacaro, E. Jimenez, E. Velez-Fort, A. Amorese, M. Aspbury, F. Yakhou-Harris, P. van der Linden, and N. B. Brookes, J. Synchrotron Radiat. **23**, 464 (2016).